Optical Identification and Spectroscopy of Supernova Remnants in the Galaxy M51

P. Frank Winkler ¹, Sadie C. Coffin ^{1,2,3,4}, William P. Blair ⁵, Knox S. Long ^{6,7}, and Kip D. Kuntz ⁵ Department of Physics, Middlebury College, Middlebury, VT 05753, USA; winkler@middlebury.edu Southeastern Universities Research Association, Washington, DC 20005, USA X-ray Astrophysics Laboratory NASA/GSFC, Greenbelt, MD 20771, USA ⁴ Center for Research and Exploration in Space Science and Technology, NASA/GSFC, Greenbelt, MD 20771, USA; sadie.coffin@nasa.gov ⁵ The Henry A. Rowland Department of Physics and Astronomy, Johns Hopkins University, 3400 N. Charles Street, Baltimore, MD 21218, USA; wblair@jhu.edu,

kkuntz1@jhu.edu ⁶ Space Telescope Science Institute, 3700 San Martin Drive, Baltimore, MD 21218, USA Eureka Scientific, Inc., 2452 Delmer Street, Suite 100, Oakland, CA 94602-3017, USA Received 2020 October 20; revised 2020 December 19; accepted 2020 December 24; published 2021 February 16

Abstract

Using a combination of ground-based and Hubble Space Telescope imaging, we have constructed a catalog of 179 supernova remnants (SNRs) and SNR candidates in the nearby spiral galaxy M51. Follow-up spectroscopy of 66 of the candidates confirms that 61 of these are SNRs and suggests that the vast majority of the unobserved objects are SNRs as well. A total of 55 of the candidates are coincident with (mostly soft) X-ray sources identified in deep Chandra observations of M51; searching the positions of other soft X-ray sources resulted in several additional possible optical candidates. There are 16 objects in the catalog coincident with known radio sources. None of the sources with spectra show the high velocities (≥500 km s⁻¹) characteristic of young, ejecta-dominated SNRs like Cas A; instead, most if not all appear to be middle-aged SNRs. The general properties of the SNRs, size distribution and spectral characteristics, resemble those in other nearby spiral galaxies, notably M33, M83, and NGC 6946, where similar samples exist. However, the spectroscopically observed [N II]:H α ratios appear to be significantly higher than in any of these other galaxies. Although we have explored various ideas to explain the high ratios in M51, none of the explanations appear to be satisfactory.

Unified Astronomy Thesaurus concepts: Supernova remnants (1667); Nebulae (1095); Interstellar medium (847); Spiral galaxies (1560)

1. Introduction

Following the violent death of a star as a supernova (SN), material rich in heavy elements is ejected and drives shock waves into the surrounding circumstellar and/or interstellar material to form a supernova remnant (SNR). SNe are a key part of the cycle that gradually enriches the cosmos; they can trigger new episodes of star formation, and collectively they may influence the evolution of the galaxies in which they take place. For understanding these processes, it is most efficacious to study SNR samples in nearby galaxies, especially spirals that are oriented nearly face-on. Here we typically find large numbers of SNRs, all at effectively the same distance, and in most cases with minimal foreground absorption. All this contrasts with our own Galaxy, where most of the hundreds of identified SNRs are at poorly determined distances and suffer from significant extinction—in many cases so much so that they have not even been detected optically.

Relatively nearby, face-on, and with well-defined spiral arms with active star formation, M51 presents an ideal venue for this study of SNRs. M51 (NGC 5194/5) has the distinction of being the first galaxy classified as a spiral (Rosse 1850) and is one of the most well-known interacting systems, comprising the granddesign spiral M51A = NGC 5194 and smaller companion M51B = NGC 5195. M51A is classified as a late-type granddesign Sbc, while its early-type northern companion M51b is classified as a barred S0. At a distance of $8.58 \pm 0.10 \, \mathrm{Mpc}$ (McQuinn et al. 2016), where 1" corresponds to a linear size of 41.6 pc, the Whirlpool Galaxy has been the site of four SNe since 1945 and is thus expected to host a rich population of SNRs.

Most extragalactic SNRs have been first identified optically, through their [S II] $\lambda\lambda$ 6716, 6731 lines, where we typically find [S II]:H α flux ratios >0.4, significantly higher than in H II regions, where [S II]:H α is usually ≤ 0.2 (e.g., Mathewson & Clarke 1973; Levenson et al. 1995; Long 2017). Most of the bright optical emission from SNRs stems from secondary shocks driven into dense clouds. The passing shock rapidly heats the material, which then gradually cools in a long-lasting postshock tail, where we find a variety of low-ionization and even neutral species that radiate following electron collisional excitation, producing optical spectra with strong forbidden lines from (especially) [S II], [N II], [O II], and [O I], in addition to Balmer lines. By contrast, the emission from HII regions stems from photoionized gas that is kept in predominantly higher ionization states by ongoing UV radiation from hot stars.

This paper presents the first catalog of SNRs in M51, derived from a combination of Hubble Space Telescope (HST) and ground-based imaging surveys. We use the traditional [S II]:H α ratio criterion to identify likely shock-heated SNR candidates.8 We also obtain and analyze spectra from many of these, along with a selection of H II regions, to better measure the [S II]: $H\alpha$ ratios, along with other low-ionization lines that characterize shock-heated SNRs. The paper is organized as follows: In Section 2 we describe our imaging observations, candidate

^{*} Based in part on observations with the NASA/ESA Hubble Space Telescope obtained at the Space Telescope Science Institute, which is operated by the Association of Universities for Research in Astronomy, Incorporated, under NASA contract NAS5-26555. Support for program Nos. 14638 and 15216 was provided through a grant from the STScI under NASA contract NAS5-26555.

Although our SNR search was limited to M51A = NGC 5194, we refer to the galaxy as M51 for simplicity.

Table 1
HST Imaging Data for M51^a

Camera	Filter	Dithers	Exp. (s)
Prog. 10452:°			
ACS/WFC	F658N	4×680	2720
ACS/WFC	F435W	4×680	2720
ACS/WFC	F555W	4×340	1360
ACS/WFC	F814W	4×340	1360
Prog. 12762:			
WFC3/UVIS	F673N	6×900	5400
WFC3/UVIS	F689M	2×500	1000

Notes.

selection, and subsequent spectroscopy. Section 3 presents the results: our complete catalog of 179 SNR candidates, and the spectra we obtained for 66 of these. In Section 4 we discuss several aspects of our results, including the unusually strong [N II] lines that dominate the spectra of many M51 SNRs, overlaps between objects in our search and ones from X-ray and radio surveys, historical SNe in M51, and the population of SNRs in M51 relative to the populations in other similar galaxies. Finally, Section 5 gives a brief summary of our conclusions.

2. Observations, Data Reduction, and Candidate Selection

M51 is the most distant galaxy for which an extensive population of SNRs has been identified (Long 2017). The most common approach for these studies, which we have followed in our own previous studies of M83 (Blair et al. 2012, 2014; Winkler et al. 2017) and NGC 6946 (Long et al. 2019, 2020), is to start with a ground-based imaging survey and follow up with HST. In the case of M51, the availability of HST data for H α and several broad bands meant that only [S II] imaging was missing in order to allow an SNR search. Hence, our observations of M51 began with narrowband imaging from HST and then continued to ground-based survey work with the 8.2 m Gemini North telescope, where we first obtained images, and then spectra for over 100 objects, all using the Gemini Multi-Object Spectrograph (GMOS). Below we describe these data sets in the order they were obtained. In reality, the order makes little difference; as with our previous studies, the ground- and spacebased survey work is largely complementary.

2.1. HST Imagery

The HST imagery used in this program is summarized in Table 1. Program GO-10452 (PI: Beckwith) was a Director's Discretionary program that used the ACS/WFC and resulted in the image of M51 that was widely distributed at the Hubble 15th anniversary. This imaging covered six overlapping ACS/WFC fields with the data from each field dithered over four exposures, resulting in the total times for each field listed in

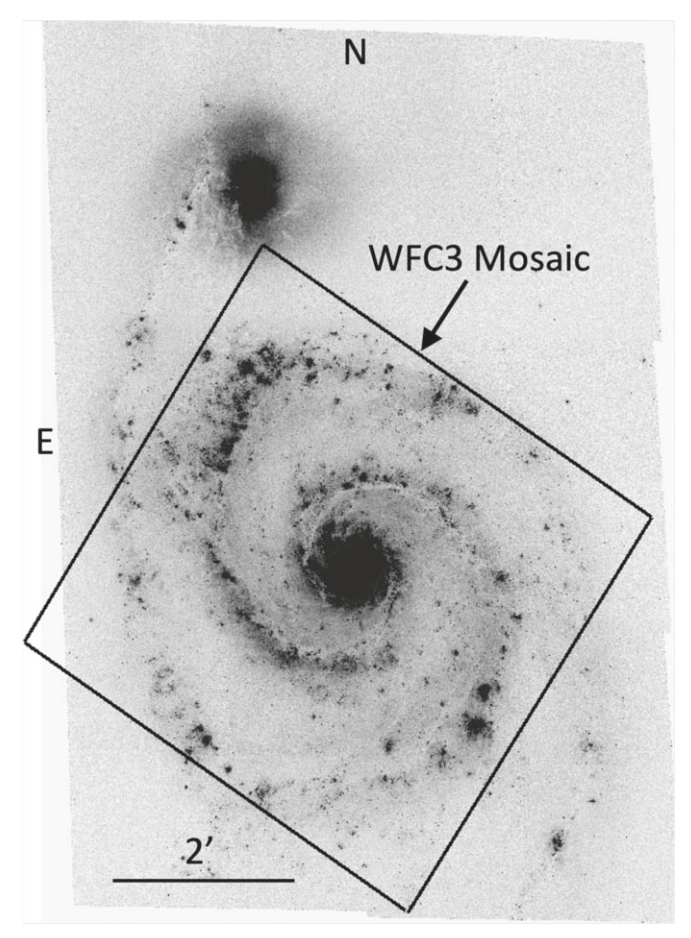


Figure 1. Relative field coverage of the HST ACS and WFC3 data. The background image is the ACS 6-field mosaic with the F658N filter. The box shows the footprint of the four-field WFC3 mosaic for comparison. WFC3 covered the main body of M51A but missed some of the outermost spiral arms. It also does not include M51B to the north.

Table 1. These observations included three broadband filters plus F658N, which captured H α (plus [N II] $\lambda\lambda$ 6548, 6583) emission from nebular regions of active star formation. These data have been used by Lee et al. (2011) for a comprehensive study of H II regions in M51 and by many other authors, but alone they are not sufficient for an SNR search, since a shock diagnostic such as [S II] $\lambda\lambda$ 6716, 6731 is also needed.

Hence, we leveraged these earlier observations by obtaining WFC3/UVIS imagery in two additional filters, also shown in Table 1. Program GO-12762 (PI: K. Kuntz) used F673N to capture [S II] $\lambda\lambda6716$, 6731 emission from four fields and used F689M to provide a continuum band for subtracting the galaxy background. These data were also dithered, to help mitigate cosmic-ray effects and chip gaps in the processed data. These data were obtained just prior to the recommendation that a pedestal of electrons (using the FLASH parameter) was advised by STScI, especially for narrowband imagery, to control charge transfer inefficiency in the CCDs. While no FLASH parameters were set, we see no obvious ill effects from not having done so. Figure 1 shows the relative field coverage of these two data sets after they were aligned and mosaicked. The newer [S II] data cover the main body of M51A but miss some of the outermost spiral arms; they do not cover the companion galaxy M51B.

All of these data were retrieved from the Mikulski Archive for Space Telescopes (MAST) for processing. The individual dither frames were aligned and combined for each field and

^a Prog. 10452 used six fields of ACS/WFC, which were obtained in 2005 January. Prog. 12762 obtained four fields of WFC3/UVIS in 2012 April; refer to Figure 1 for relative field coverage.

Exposure time for each field including all dithers.

c A MAST High Level Science Program for these data can be found at https://archive.stsci.edu/prepds/m51/.

⁹ See https://hubblesite.org/contents/media/images/2005/12/1677-Image.html?Topic=105-galaxies&keyword=M51&news=true, and also 10.17909/T9GP4C for the underlying data.

then placed into a mosaic. Since the native pixel scales are different for ACS and WFC3, we used the AstroDrizzle package (Fruchter et al. 2010; Gonzaga et al. 2012) to produce aligned mosaics on a common grid that allows direct comparison. The procedure closely followed that described in Blair et al. (2014; see Section 2 and the Appendix of that paper) for M83 and will not be repeated here. Astrometric alignments relied on centroids of isolated stars in the overlap regions between fields of the mosaic to align all of the frames to a single grid and then used stars from the UCAC3 astrometric catalog (Zacharias et al. 2010) and the Two Micron All Sky Survey, selecting objects with small positional uncertainties and checking visually to eliminate close doubles and a few background galaxies. ^{fo} Finally, the WCS keywords in the FITS file headers were adjusted to place the entire data set on the same absolute astrometric scale, with relative alignment accurate to <0.1''1.

Once the images were mosaicked and aligned, the initial search process was straightforward. We used standard IRAF¹¹ techniques to scale and subtract continuum from the emission-line images. After some experimentation, we ultimately used the ACS F555W continuum image to scale and subtract from both the H α and [S II] mosaics. This choice provided a subtraction of the H α image over the entire ACS mosaic area, though our [S II] coverage was more restricted. The color differences between the galaxy background in the nuclear region and the outer arms made it difficult to use a single scaling of the continuum image for subtraction, so a separate subtraction (that oversubtracted the outer galaxy) was used specifically for the inner portion of the galaxy.

The search procedure was to simultaneously display the subtracted $H\alpha$ and [S II] frames along with a continuum band for reference using SAOimage DS9 (Joye & Mandel 2003). Subregions of the WFC3 mosaic were then enlarged to an appropriate scale and inspected visually to locate compact emission nebulae with enhanced [S II] emission. Comparison against the continuum frame prevented us from mistaking stellar residuals for possibly interesting compact nebulae. Cursor readings could be used to estimate the observed ratio of [S II] to $H\alpha$. Figure 2 shows an example of a small region containing several SNR candidates as an example, including a color image that also highlights the different relative line intensities for the nebulae in the region shown.

A significant caveat that made this process less determinative than in previous galaxy searches was that the ACS filter used for H α (F658N) was broad enough to fully include the [N II] lines that bracket H α . [N II] is both strong and variable in M51, especially in the SNRs (a fact later confirmed with our spectroscopy), effectively making the images a comparison of the [S II]:(H α + [N II]) instead of [S II]:H α . This had the effect of decreasing the contrast between the ratio for SNRs and H II regions that we normally depend on to identify the SNRs. Nonetheless, with appropriate scaling, a set of compact nebulae that were relatively strong in [S II] could be identified, as illustrated by the example shown in Figure 2. The overall blind search of the HST data resulted in 80 compact nebulae that

were judged to have observed ratios significantly elevated over what was typical for obvious H II regions, but with somewhat less certainty as to their quality as SNR candidates than had been the case for our previous surveys of other galaxies. The spatial distribution of these objects across the region observed is shown by the yellow circles in Figure 3.

Circular DS9 regions were set on these objects and resized to provide a measurement of both the position and the angular size of each object. Although some objects show some extent and morphology in the HST data (see Figure 2), these objects are almost all below 1'' in size, extending down almost to the resolution limit of the WFC3 data for the smallest nebulae. (Note: one WFC3 pixel = 0.''04, or \sim 2 pc at the distance of M51.)

2.2. GMOS-N Images

Although the exquisite resolution of the HST WFC3 images enabled us to identify these small objects of interest, the exposures were not deep enough to see larger, lower surface brightness (and presumably older) SNRs. Hence, as a complement to the HST survey, we received approval for imaging M51 with the GMOS on the 8.2 m Gemini North telescope through the "Fast Turnaround" program GN-2017A-FT-7 (PI: Long). Through this program, we obtained narrowband images of two overlapping fields covering most of M51 with GMOS in three bands: H α , [S II], and a matched continuum band (HaC filter). The observing details are given in Table 2.

We processed these images using standard IRAF techniques in the gmos package, using dozens of stars from Gaia DR2 (Gaia Collaboration et al. 2018) to improve the World Coordinate system, and mosaicked the two fields together. To enhance the search for faint nebulae, it is useful to use continuum-subtracted images, obtained by scaling and subtracting the continuum image (separately) from the H α and [S II] layers. Finally, we flux-calibrated the continuum-subtracted images, using short H α and [S II] observations of two spectrophotometric standards from the list of Massey et al. (1988).

Unfortunately, this procedure was not efficacious for the [S II] images of M51, because at the 600 km s⁻¹ redshift of M51 the [N II] λ 6584 line was shifted well into the bandpass of the HaC filter, with a transmission of almost 50%. Since (as we later discovered through our spectroscopy) the [N II] lines are extremely strong in many M51 SNRs, subtracting the "continuum" effectively removed much of the nebular emission along with the stars. We had, in effect, "thrown out the baby with the bath water"! To search for SNR candidates, we thus displayed the *unsubtracted* flux-calibrated H α and [S II] images in DS9, carefully compared small regions, and marked nebulae that appeared to have a relatively strong [SII]: $H\alpha$ ratio when compared to obvious H II regions. While this ersatz procedure was less stringent than using continuum-subtracted images, as we have done for similar searches in other galaxies, we were nevertheless able to identify 107 SNR candidates from the GMOS images. After eliminating duplicates with candidates already identified from the HST images, this left 71 new candidates from the GMOS search alone, and a total of 151 from both HST and GMOS. All of these are listed in Table 3. In order to establish priorities to use in designing masks for our subsequent multiobject spectroscopy, we assigned each of these a confidence grade of A, B, or C, based on their [S II]: $H\alpha$

 $[\]overline{^{10}}$ This work was done prior to the availability of the Gaia data, and since it is more than accurate enough for our present purposes, the astrometry has not been revisited.

¹¹ IRAF is distributed by the National Optical Astronomy Observatories, which are operated by the Association of Universities for Research in Astronomy, Inc., under cooperative agreement with the National Science Foundation.

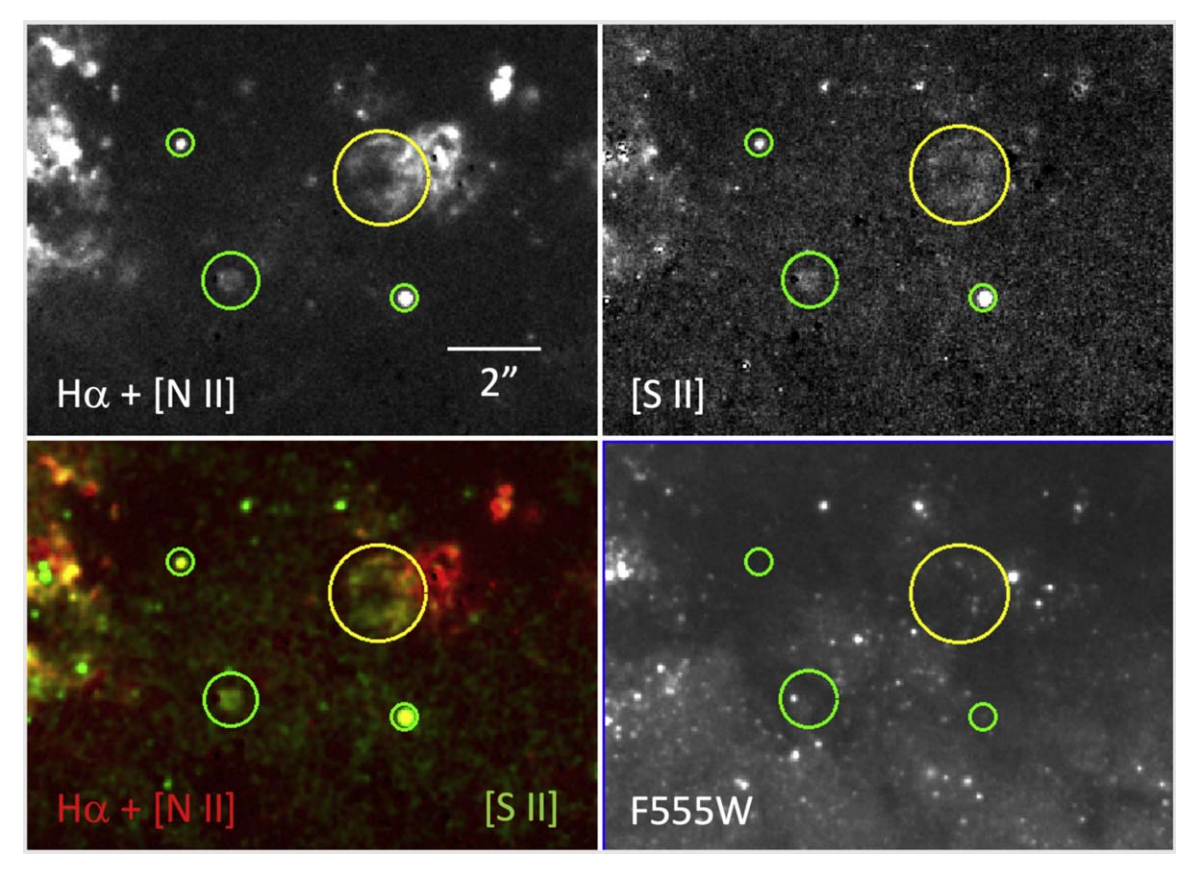


Figure 2. HST image data for a small region, located in the first spiral arm south of the nucleus, that contains four SNR candidates. The region is centered at R.A. (J2000) = 13:29:55.93, decl.(J2000) = +47:10:45.4 and is oriented north up, east to the left. The green circles indicate three candidates identified in our blind search of the HST images, where we looked for compact nebulae with elevated [S II]:H α ratios. The H α + [N II] and [S II] panels have been continuum-subtracted using the F555W data shown at lower right. The color panel has been scaled to show the SNR candidates as green to yellow, while photoionized regions appear as red. The yellow circle indicates a large-diameter, low surface brightness SNR candidate found in the ground-based search that was later corroborated by the HST data when an appropriate display stretch was used. For scale, the object in the largest green circle is approximately half the size of the Cygnus Loop in our Galaxy.

ratio as estimated from the images, morphology, and lack of confusion with surrounding emission.

Subsequent to our spectroscopy, we made another careful pass through both the GMOS and the HST images to search for additional candidates that might have been missed earlier. The GMOS search was aided by the late acquisition of broad *r*-band images of exactly the same fields we had imaged previously using narrowband filters. By precisely aligning the *r*-band images with those in [S II], we were at last able to make useful continuum-subtracted [S II] images. ¹² In these improved images, the candidates we had selected earlier became more obvious, and several new candidates appeared as well. Our later search of both HST and GMOS images yielded 28 new candidates, which we have also included in Table 3 for a grand total of 179.

2.3. GMOS-N Spectroscopy

We pursued follow-up multiobject spectroscopy from GMOS-N under program GN-2018A-Q-302 (PI: Winkler). Based on the spatial distribution of SNR candidates, we determined that masks with slits oriented north-south would

give greater efficiency than an east—west orientation, which would have been required had we used our 2017 GMOS images for mask design. Therefore, we did short dithered exposures in the broad *r* filter of two overlapping M51 fields with the GMOS chips oriented N–S, which we then used as pre-images to design the MOS masks.

Three masks were designed and observed, giving preference to higher graded candidates; in total, these included 44 "A" candidates, 18 "B" candidates, and 3 "C" candidates, plus one additional SNR that appeared serendipitously on one of the slits: 13 a total of 66 SNR candidates with spectra. The locations of all the SNR candidates with spectra are indicated by the red squares in Figure 3. In addition, we explicitly targeted a number of H II regions and obtained spectra for several others that serendipitously lay along slits with other targets: a total of 44 H II regions spanning a wide range in location, surface brightness, and size. We list these H II regions in Table 4.

Our GMOS-N program used the B600 grating (G5307, 600 lines mm $^{-1}$) and GG455 blocking filter, with the Hamamatsu detector binned $\times 4$ in the dispersion direction, and $\times 2$ spatially, to give a dispersion of 2.06 Å pixel $^{-1}$ and a spatial scale of 0.16 pixel $^{-1}$. The spectral coverage varied with the

 $[\]overline{^{12}}$ The broad r filter passes H α , [N II], and [S II] lines, but its far greater bandwidth (1360 Å, compared with \sim 40–70 Å for the emission-line filters) makes it relatively more sensitive to stars, and thus effective for continuum subtraction.

¹³ Subsequent inspection of the HST images showed that this was clearly a strong candidate that we had overlooked in our initial search; henceforth, we count it among the "A" candidates.

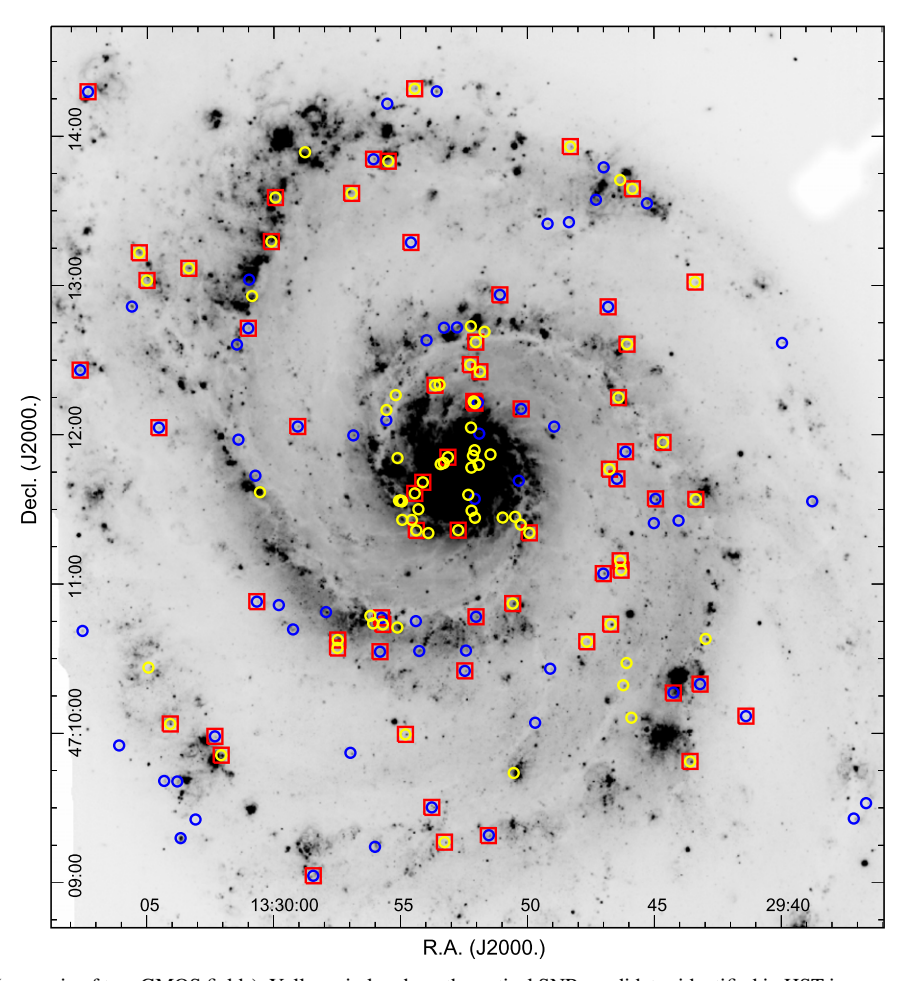


Figure 3. $H\alpha$ image of M51 (a mosaic of two GMOS fields). Yellow circles show the optical SNR candidates identified in HST images; blue circles are ones identified in GMOS images. Candidates for which we obtained spectra are indicated by the slightly larger red squares. As the figure indicates, candidates with spectra are well distributed around the galaxy.

Table 2
GMOS Imaging Observations of M51

	R.A.	Decl.			Fi	lter	Exposure
Field	(J20	000.)	Date	Designation	$\lambda_{\rm c}$ (Å)	$\Delta \lambda (\mathring{A})^{a}$	(s)
				$H\alpha$	6573	72	6 × 350
M51 North	13:29:53.0	47:13:40.8	2017 Mar 27	HaC	6642	69	6×440
				[S II]	6718	43	6×500
			2018 Jun 2	r	6300	1360	6×60
				$_{ m Hlpha}$	6573	72	6×350
M51 South	13:29:51.0	47:10:10.0	2017 May 21	HaC	6642	69	6×440
				[S II]	6718	43	6×500
			2018 Jun 2	r	6300	1360	6×60

Note.

position of the object, but for almost all the objects coverage extended at least from H β through [S II] $\lambda\lambda$ 6716, 6731, with a resolution of about 5.2 Å. Spectra were then taken with each of the three masks in 2018 May–July. For each mask, four exposures of 1100 s each were acquired at each of three grating tilts, giving three central wavelength (CWL) settings, 5800, 5900, and 6000 Å, to assure that gaps in spectral coverage (resulting from the chip gaps on the GMOS detector) would be

fully covered.¹⁴ Immediately before or after the science frames at each CWL setting, quartz flat and CuAr arc calibration frames were obtained.

The data were processed using standard procedures from the gemini package in IRAF for bias subtraction, flat-fielding,

^a FWHM.

 $[\]overline{^{14}}$ An exception is mask 3, where four $\overline{1100}$ s exposures were obtained at 5800 and 5900 Å, but only two 1100 s exposures at 6000 Å.

Table 3 SNR Candidates in M51

SNR Candidates in M51										
Name	R.A. (J2000)	Decl. (J2000)	Diam. (pc)	R (kpc)	X-Ray	Radio	Spec.	[S II]: $\mathrm{H}\alpha > 0.4$		
W21-001	13:29:37.05	47:09:25.5	27	9.0	•••		n			
W21-002	13:29:37.34	47:10:07.6	54	7.9	•••	•••	n	•••		
W21-003	13:29:38.77	47:11:33.3	100	6.3		•••	n	•••		
W21-004 ^a	13:29:39.96	47:12:37.1	45	6.2	X107	•••	n	•••		
W21-005 W21-006	13:29:41.24 13:29:41.39	47:08:13.4 47:10:06.9	50 32	10.0 6.4		•••	n			
W21-000 W21-007	13:29:41.69	47:10:00.9	32 47	10.6			y n	n 		
W21-007	13:29:42.42	47:07:42.5	92	10.9		•••	n	•••		
W21-009	13:29:42.97	47:10:38.0	21	5.1	X123		n			
W21-010	13:29:43.19	47:10:19.8	53	5.4	•••		y	n		
W21-011 ^b	13:29:43.36	47:11:34.1	12	4.2	X124		y	y		
W21-012	13:29:43.38	47:13:01.4	23	5.4	•••	•••	y	y		
W21-013	13:29:43.59	47:09:48.7	30	6.2	•••	•••	y	y		
W21-014	13:29:43.98	47:12:23.2	34	4.3		•••	n	•••		
W21-015	13:29:44.01	47:11:51.0	20	4.0	•••	•••	n	•••		
W21-016	13:29:44.04	47:11:25.5	44	4.0	•••	•••	n	•••		
W21-017	13:29:44.25	47:10:16.2	15	5.2	•••	•••	У	У		
W21-018	13:29:44.40	47:11:40.1	32	3.7	•••	•••	n	•••		
W21-019 W21-020	13:29:44.56 13:29:44.65	47:11:40.3 47:11:57.0	44 29	3.7 3.7	***	•••	n	•••		
W21-020 W21-021	13:29:44.05	47:11:37.0	29 18	3.7			у	у		
W21-021 W21-022	13:29:45.01	47:11:34.5	35	3.5 3.5	•••		y n	n 		
W21-022 W21-023	13:29:45.28	47:13:33.1	27	5.8			n			
W21-024	13:29:45.90	47:10:06.3	27	5.0		•••	n	•••		
W21-025	13:29:46.07	47:12:36.5	26	3.8			y	у		
W21-026	13:29:46.09	47:10:28.3	30	4.2			n			
W21-027	13:29:46.13	47:11:53.2	51	3.0	•••		y	y		
W21-028	13:29:46.22	47:10:19.4	29	4.5			n			
W21-029	13:29:46.30	47:11:05.6	23	3.2			y	y		
W21-030	13:29:46.32	47:08:38.4	82	8.2	•••	•••	n	•••		
W21-031	13:29:46.34	47:13:42.5	7	5.8	•••	•••	n	•••		
W21-032	13:29:46.34	47:11:09.4	17	3.2	X144	•••	У	У		
W21-033	13:29:46.40	47:12:15.0	18	3.2	•••	•••	у	у		
W21-034	13:29:46.47	47:11:42.3	37	2.8	•••	•••	У	у		
W21-035	13:29:46.72	47:10:43.9	33	3.6	•••	•••	У	У		
W21-036 W21-037	13:29:46.72 13:29:46.76	47:08:36.8 47:11:46.2	49 35	8.2 2.7	•••		n			
W21-037 W21-038	13:29:46.81	47:11:40.2	32	4.0			y	У		
W21-038 W21-039	13:29:46.99	47:12:31:3	39	5.9			y n	у 		
W21-039	13:29:47.01	47:11:04.2	24	3.0	X149		y	y		
W21-041	13:29:47.29	47:13:34.5	31	5.3			n			
W21-042	13:29:47.66	47:10:36.9	25	3.5			y	y		
W21-043	13:29:48.10	47:09:29.3	43	5.9	•••		n			
W21-044	13:29:48.30	47:13:55.9	17	6.0			y	y		
W21-045	13:29:48.36	47:13:25.5	24	4.8			n			
W21-046	13:29:48.36	47:09:42.7	53	5.3	•••	•••	n	•••		
W21-047	13:29:48.94	47:12:03.3	66	1.9	•••	•••	n	•••		
W21-048	13:29:49.10	47:10:26.0	29	3.5		•••	n	•••		
W21-049	13:29:49.20	47:13:24.9	26	4.6	•••	•••	n	•••		
W21-050	13:29:49.69	47:10:04.3	37	4.3			n	•••		
W21-051	13:29:49.92	47:11:20.6	21	1.5	X161	M07-017	У	у		
W21-052	13:29:50.24	47:12:10.5	22	1.6	X166	•••	у	у		
W21-053	13:29:50.26	47:11:23.9	7	1.3	 V160	•••	n	•••		
W21-054 W21-055	13:29:50.34 13:29:50.48	47:11:41.6 47:11:27.1	36 9	1.1 1.2	X169 X171	 M07-031	n n	•••		
W21-055 W21-056	13:29:50.54	47:11:27.1	19	5.0	X1/1 	MIO7-051	n	•••		
W21-050 W21-057	13:29:50.54	47:11:44.6	24	1.0	X170		n			
W21-057	13:29:50.58	47:10:52.2	29	2.3	X170 X172		y	у		
W21-059	13:29:50.98	47:11:26.8	12	1.0	X177		n			
W21-060	13:29:51.08	47:12:56.3	27	3.2			y	у		
W21-061	13:29:51.45	47:11:52.1	13	0.7	X180		n			
W21-062	13:29:51.54	47:09:18.9	34	6.0			y	n		
W21-063	13:29:51.69	47:12:41.5	19	2.5	•••		n	•••		

Table 3 (Continued)

(Continued)										
Name	R.A. (J2000)	Decl. (J2000)	Diam. (pc)	R (kpc)	X-Ray	Radio	Spec.	[S II]: $H\alpha > 0.4$		
W21-064	13:29:51.87	47:12:25.4	13	1.8	X187	•••	у	y		
W21-065	13:29:51.90	47:12:00.5	21	0.8	•••	•••	n			
W21-066	13:29:51.92	47:11:48.0	13	0.4	•••	•••	n	•••		
W21-067	13:29:51.95	47:12:13.0	18	1.3	•••	•••	n			
W21-068	13:29:52.02	47:10:46.9	26	2.3	X189	•••	y	y		
W21-069	13:29:52.03	47:12:37.3	16	2.3	•••	•••	y	У		
W21-070	13:29:52.07	47:12:12.8	13	1.3	X192	•••	y	У		
W21-071	13:29:52.07	47:11:26.7	17	0.7	X191	M07-047	n	•••		
W21-072	13:29:52.07	47:11:34.3	59	0.5	•••	•••	n	•••		
W21-073	13:29:52.08	47:11:53.9	16	0.6		•••	n	•••		
W21-074	13:29:52.11	47:12:13.5	20	1.3	X192	•••	У	У		
W21-075	13:29:52.15	47:11:51.6	10	0.5	 V106	 M07.040	n	***		
W21-076 W21-077	13:29:52.20 13:29:52.21	47:11:29.6 47:11:46.9	12 13	0.6 0.3	X196 	M07-049 	n	•••		
W21-077 W21-078	13:29:52.22	47:11:40.9	13	0.9	X194		n	•••		
W21-078 W21-079	13:29:52.23	47:12:43.7	9	2.5			n	•••		
W21-079 W21-080	13:29:52.25	47:12:28.2	22	1.9	X199		n			
W21-080	13:29:52.29	47:12:28:2	10	0.7			y n	у 		
W21-081 W21-082	13:29:52.33	47:11:35.9	13	0.7		M07-050	n	•••		
W21-082 W21-083	13:29:52.42	47:10:33.3	39	2.9			n			
W21-083	13:29:52.47	47:10:25.2	22	3.2	•••		y			
W21-085	13:29:52.73	47:11:21.7	16	0.9	X208	M07-052	y	У		
W21-085	13:29:52.78	47:12:43.2	66	2.5			n n	у 		
W21-087	13:29:53.00	47:11:42.3	7	0.1	•••	•••	n	•••		
W21-088	13:29:53.13	47:11:51.0	11	0.4			у	y		
W21-089	13:29:53.27	47:09:16.3	18	6.1			y	y		
W21-090	13:29:53.29	47:12:43.1	23	2.5			n			
W21-091	13:29:53.42	47:11:48.3	29	0.4			n	•••		
W21-092	13:29:53.46	47:12:20.2	19	1.6			n			
W21-093	13:29:53.58	47:14:18.1	34	6.5			n			
W21-094	13:29:53.64	47:12:20.0	17	1.6			y	y		
W21-095	13:29:53.77	47:09:30.3	75	5.6	•••	•••	y	y		
W21-096	13:29:53.96	47:09:23.5	12	5.8	X235	•••	n			
W21-097	13:29:53.98	47:12:38.1	31	2.4	•••		n	•••		
W21-098	13:29:54.12	47:11:41.0	12	0.6			y	y		
W21-099	13:29:54.26	47:10:33.1	49	3.0			n			
W21-100	13:29:54.30	47:11:30.1	11	0.9	X242	M07-061	n			
W21-101	13:29:54.38	47:11:21.6	12	1.2	X243		y	y		
W21-102	13:29:54.40	47:10:45.2	36	2.5			n			
W21-103	13:29:54.44	47:11:36.5	18	0.8	X245	•••	y	y		
W21-104	13:29:54.44	47:14:19.1	17	6.5	X246	•••	y	y		
W21-105	13:29:54.55	47:11:25.8	11	1.1	•••	•••	n	•••		
W21-106	13:29:54.59	47:13:17.3	26	4.0	X249	•••	y	у		
W21-107	13:29:54.66	47:09:35.4	40	5.4	•••	•••	n	•••		
W21-108	13:29:54.81	47:09:59.6	12	4.4	X252	•••	y	y		
W21-109	13:29:54.93	47:11:25.9	12	1.2	X256	•••	n	•••		
W21-110	13:29:54.94	47:11:33.3	15	1.1	X259	M07-064	n	•••		
W21-111	13:29:54.98	47:11:33.6	9	1.1	X259	M07-064	n	•••		
W21-112	13:29:55.06	47:11:33.6	9	1.1	X259	•••	n	•••		
W21-113	13:29:55.12	47:11:50.7	22	1.1	X261	•••	n	•••		
W21-114	13:29:55.12	47:10:42.6	9	2.8	X262	•••	n	•••		
W21-115	13:29:55.19	47:12:16.0	22	1.8	X264	•••	n	•••		
W21-116	13:29:55.21	47:09:36.1	48	5.4			n	•••		
W21-117	13:29:55.24	47:10:46.5	18	2.6	X265	M07-068	n	•••		
W21-118	13:29:55.49	47:13:50.0	21	5.4	•••	•••	У	У		
W21-119	13:29:55.53	47:14:13.1	39	6.4			n	•••		
W21-120	13:29:55.56	47:12:10.0	22	1.7	X274	M07-074	n	•••		
W21-121	13:29:55.56	47:12:05.9	37 47	1.6	•••	•••	n	***		
W21-122	13:29:55.68	47:09:28.2	47	5.8	 V277	•••	n	•••		
W21-123	13:29:55.70	47:10:43.8	14	2.8	X277	•••	у	у		
W21-124	13:29:55.75	47:10:46.5	66 52	2.8	X278	•••	у	n		
W21-125	13:29:55.81	47:10:32.9	52	3.3	•••	•••	У	у		

Table 3 (Continued)

Name	R.A. (J2000)	Decl. (J2000)	Diam. (pc)	R (kpc)	X-Ray	Radio	Spec.	[S II]: $\mathrm{H}\alpha > 0.4$
W21-126	13:29:55.86	47:11:44.7	17	1.4	X279	M07-079	n	
W21-127	13:29:56.01	47:09:14.4	50	6.4			n	
W21-128	13:29:56.07	47:13:50.8	11	5.5	X281		y	y
W21-129	13:29:56.08	47:10:44.2	20	2.9			n	
W21-130	13:29:56.19	47:10:47.3	11	2.8	X283	M07-083	n	•••
W21-131	13:29:56.86	47:11:59.8	13	2.0			n	•••
W21-132	13:29:56.93	47:13:37.1	20	5.1			y	y
W21-133	13:29:56.97	47:09:52.2	47	5.0			n	
W21-134	13:29:57.48	47:10:37.6	26	3.5	X293	M07-084	y	y
W21-135	13:29:57.49	47:10:34.3	32	3.6			y	y
W21-136	13:29:57.72	47:09:06.6	61	7.0			n	
W21-137	13:29:57.94	47:10:48.8	29	3.3			n	
W21-138	13:29:58.26	47:09:05.7	24	7.1			n	
W21-139	13:29:58.44	47:09:02.8	24	7.2			y	y
W21-140	13:29:58.44	47:14:03.8	7	6.4			n	
W21-141	13:29:58.77	47:13:53.6	20	6.0			n	
W21-142	13:29:59.05	47:12:03.4	30	3.0	X313		y	y
W21-143	13:29:59.24	47:10:41.8	51	3.9			n	
W21-144	13:29:59.34	47:10:41:8	147	4.1	•••	•••	n	•••
W21-144 W21-145	13:29:59.73	47:12:31:0	53	4.5			n	
W21-145 W21-146	13:29:59.80	47:10:51.6	49	3.9	•••	•••	n	•••
W21-140 W21-147	13:29:59.94	47:10:31.6	18	5.7	•••			
W21-147 W21-148	13:30:00.10	47:13:33.4	12	5.1			у	y
W21-146 W21-149	13:30:00.10	47:13:17.7	36	4.1			У	У
					•••	•••	n	•••
W21-150	13:30:00.44	47:09:15.2	52	7.2	 V226	•••	n	•••
W21-151	13:30:00.54	47:11:36.9	20	3.5	X326	•••	n	
W21-152	13:30:00.67	47:10:53.0	35	4.2	•••	•••	У	У
W21-153	13:30:00.72	47:11:43.6	30	3.6	•••	•••	n	•••
W21-154	13:30:00.86	47:12:55.8	17	4.7		•••	n	•••
W21-155	13:30:01.01	47:12:42.9	17	4.5	X335		У	У
W21-156	13:30:01.39	47:11:58.1	12	4.0	X339	M07-096	n	•••
W21-157	13:30:01.40	47:12:01.5	28	4.0	•••	•••	n	•••
W21-158	13:30:01.45	47:12:36.3	54	4.5	•••	•••	n	•••
W21-159	13:30:01.52	47:12:41.1	17	4.6	•••	•••	n	•••
W21-160	13:30:01.99	47:10:31.2	24	5.2	•••	•••	n	•••
W21-161	13:30:02.07	47:09:51.2	23	6.4	X347	M07-099	У	У
W21-162	13:30:02.32	47:09:58.8	38	6.2	X349	•••	У	У
W21-163	13:30:03.08	47:09:25.4	27	7.5		•••	n	•••
W21-164	13:30:03.35	47:13:06.9	21	5.9	X352	•••	у	y
W21-165	13:30:03.66	47:09:17.9	71	7.9	X354	•••	n	•••
W21-166	13:30:03.80	47:09:40.7	58	7.2	•••	•••	n	•••
W21-167	13:30:04.08	47:10:03.8	12	6.7	X357	•••	y	y
W21-168	13:30:04.32	47:09:40.9	60	7.4	•••	•••	n	•••
W21-169	13:30:04.53	47:12:02.9	40	5.4	X363	•••	y	y
W21-170	13:30:04.77	47:13:01.2	18	6.3	•••	•••	n	•••
W21-171	13:30:04.94	47:10:26.4	34	6.4			n	
W21-172	13:30:05.00	47:13:02.0	14	6.4	X366		y	у
W21-173	13:30:05.31	47:13:13.2	32	6.7			y	y
W21-174	13:30:05.65	47:12:51.8	17	6.4		•••	n	
W21-175	13:30:06.09	47:09:55.1	80	7.6		•••	n	
W21-176	13:30:06.79	47:12:10.3	40	6.4			n	
W21-177	13:30:07.34	47:14:17.9	29	9.1			y	y
W21-178	13:30:07.54	47:10:41.1	44	7.2			n	
W21-179	13:30:07.64	47:12:26.0	17	6.9			y	n

Notes.

^a This object corresponds with ULX-1 reported by Urquhart et al. (2018); the object is distinctly elongated and is likely a jet-like structure. The listed diameter

corresponds to the long dimension of the observed nebula.

b This object corresponds with source 5 in Terashima & Wilson (2004) and is likely also source ULX-2 reported by Brightman et al. (2020); the listed coordinate in the latter reference is off, but inspection of Chandra data shows that the strong X-ray source near this position actually aligns with W21-011.

Table 4
H II Regions in M51

Name	R.A. (J2000)	Decl. (J2000)	R (kpc)	X-Ray	Radio
HII-01	13:29:39.31	47:08:40.4	9.6	•••	M07-005
HII-02	13:29:39.38	47:08:35.9	9.7	•••	
HII-03	13:29:43.14	47:10:21.4	5.4	•••	•••
HII-04	13:29:43.18	47:10:24.3	5.3	•••	•••
HII-05	13:29:43.23	47:10:26.0	5.3	•••	•••
HII-06	13:29:43.66	47:09:51.0	6.1	•••	•••
HII-07	13:29:43.73	47:13:08.3	5.5	•••	•••
HII-08	13:29:43.77	47:13:10.1	5.5	•••	•••
HII-09	13:29:44.12	47:10:22.9	5.0	X130	M07-007
HII-10	13:29:44.46	47:10:58.6	4.1	•••	
HII-11	13:29:44.50	47:10:55.6	4.2	•••	
HII-12	13:29:44.65	47:11:54.9	3.7	•••	• • • •
HII-13	13:29:44.91	47:11:32.2	3.5	•••	•••
HII-14	13:29:45.86	47:13:41.8	5.9	•••	•••
HII-15	13:29:45.86	47:13:32.3	5.6	•••	•••
HII-16	13:29:46.10	47:12:34.3	3.7	•••	
HII-17	13:29:46.31	47:12:17.6	3.3	•••	
HII-18	13:29:46.33	47:11:07.8	3.2	•••	
HII-19	13:29:46.39	47:12:11.8	3.1	•••	
HII-20	13:29:47.15	47:08:52.1	7.5	•••	
HII-21	13:29:48.02	47:10:17.2	4.1		
HII-22	13:29:49.27	47:09:25.9	5.9		
HII-23	13:29:49.95	47:11:24.4	1.4	X162	
HII-24	13:29:51.07	47:12:53.1	3.0		
HII-25	13:29:52.02	47:12:32.5	2.1		
HII-26	13:29:52.08	47:12:45.2	2.6	X193	
HII-27	13:29:52.79	47:11:23.6	0.9		
HII-28	13:29:52.80	47:14:07.3	6.0		
HII-29	13:29:53.24	47:09:32.6	5.4		
HII-30	13:29:54.87	47:10:04.2	4.2		
HII-31	13:29:55.51	47:13:47.2	5.3		
HII-32	13:29:55.59	47:13:52.3	5.5		
HII-33	13:29:57.26	47:09:18.7	6.4		
HII-34	13:29:59.26	47:13:44.6	5.8		
HII-35	13:29:59.70	47:13:58.6	6.4	X319	
HII-36	13:30:00.93	47:09:29.6	6.8		M07-094
HII-37	13:30:01.43	47:09:03.5	7.8		
HII-38	13:30:02.36	47:09:49.6	6.5		M07-100
HII-39	13:30:03.41	47:12:53.8	5.6		
HII-40	13:30:03.47	47:09:41.2	7.1	•••	M07-102
HII-40	13:30:05.00	47:13:03.7	6.4		
HII-41	13:30:07.12	47:13:57.8	8.5		
HII-43	13:30:07.12	47:13:37.8	8.8		
HII-44	13:30:07.23	47:14:07.3	8.8 7.7		M07-105
HII-45	13:30:07.41	47:13:21.9	9.1		WI07-103
1111-43	13.30.07.43	47.14.14.0	7.1	•••	•••

wavelength calibration, and combination of spectra with different CWL settings to provide the final two-dimensional spectra. Flux calibration was based on baseline GMOS observations of a few spectrophotometric standard stars, carried out in the same semester as part of standard GMOS operations.

During the processing, the 2D spectra from different slitlets were separated to give individual 2D spectra from each slitlet. We examined each of these individually to determine the optimum background sky subtraction region. Many of the objects are located in regions with bright surrounding galactic background (both continuum and emission lines) from M51, so the ability to subtract a representative local background in the vicinity of each object is important for obtaining accurate spectra. In most cases this limited the precision of our eventual line flux measurements. Finally, we summed rows containing

each object to yield our final one-dimensional spectra. Several typical examples are shown in Figure 4.

We then performed fits to obtain emission-line fluxes from the spectra, assuming Gaussian profiles, for the following lines and line complexes: H β alone, the [O III] doublet, the [O I] doublet, the H α -[N II] complex, and the [S II] doublet. For the fits, we assumed that the background varied linearly with wavelength around each line or complex, and that the FWHM of all lines in each complex was the same.

3. Results

Table 5 lists the information we obtained for the SNR candidates for which we obtained spectra. Specifically we list (1) the source name, (2) the extracted $H\alpha$ flux, (3–9) the fluxes of primary emission lines, relative to $H\alpha=300$, and (10) the total [S II]: $H\alpha$ ratio. For doublets where the line ratio is constrained by atomic physics, i.e., [O III], [O I], and [N II], we have listed only the stronger line. We visually inspected all the spectra and the fits to them; values that we judged to be more uncertain are indicated by a tilde in the table. No allowance has been made for additional uncertainties associated with background sky subtraction. A few objects were observed with two different masks; in these cases, we used the spectrum that we judged to be of higher quality. Table 6 lists the same information for the H II region spectra.

The left panel of Figure 5 shows a plot of the [S II]: $H\alpha$ ratio for all the objects for which we obtained spectra. Of the 66 SNR candidates with spectra, we measured [S II]: $H\alpha$ ratios >0.4 for 60 of them, leading us to conclude that these may be considered bona fide SNRs. (This number includes 43 of the 44 "A" candidates we observed, and 15 of the 18 "B" ones.) Furthermore, of these 60 with strong [S II]: $H\alpha$ ratios, 56 also show clear evidence for [O I] $\lambda 6300$ emission—another strong indicator of shock excitation. So too does one of the candidates with a marginal [S II]: $H\alpha$ ratio; hence, we conclude that there are at least 61 bona fide SNRs in our sample. The five candidates not yet confirmed are W21-006, W21-021, W21-062, W21-124, and W21-179. While we cannot confirm that these objects are SNRs, neither can we conclude the opposite, since coincident photoionized gas could dilute emission from SNR shocks. Instead, these remain SNR candidates.

4. Discussion

4.1. Unusually Strong Forbidden Lines

The most noticeable features of our M51 SNR spectra are the extremely strong [N II] $\lambda\lambda6548$, 6583 lines and, to a lesser extent, the [S II] $\lambda\lambda$ 6716, 6731 lines, both with respect to H α . Other spiral galaxies with rich SNR populations, e.g., M33 (Long et al. 2018), M81 (Matonick & Fesen 1997; Lee et al. 2015), M83 (Winkler et al. 2017), M101 (Matonick & Fesen 1997), and NGC 6946 (Long et al. 2019), show a similar effect, but it is more extreme in M51. In fact, in a few cases the weaker [N II] λ 6548 line is stronger than $H\alpha$ —something we are unaware of in SNRs from any of the other galaxy samples. As shown in Figure 6, the [N II] lines are significantly stronger for smaller remnants, and they also show a strong gradient with increasing galactocentric distance (GCD; listed as R in the tables), albeit with very significant dispersion among objects. Figure 7 shows a similar but less extreme effect seen in the [S II]: $H\alpha$ ratio. The SNRs with the most extreme [N II]:H α ratios, all >3.5, are W21-088, W21-064, W21-074, W21-106, W21-085, and W21-051. These are all near the center of M51: five of the six have R < 2 kpc, and the sixth,

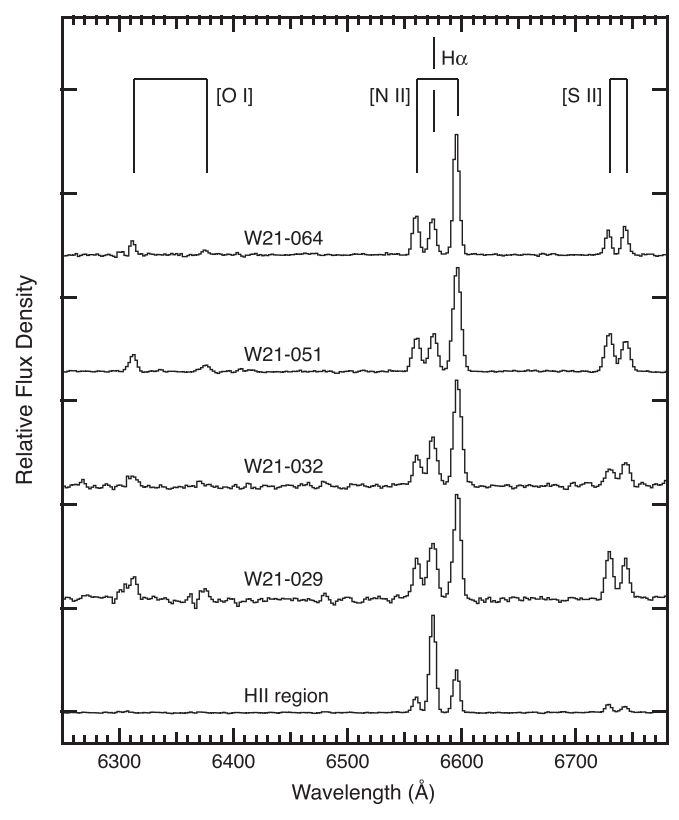


Figure 4. Several examples of the SNR spectra we obtained, as well as one H II region spectrum. The lower three spectra were all objects on the same slit.

W21-106, is at R=4.0 kpc. All are relatively small, D<26 pc, and all have [S II]:H α ratios >1.29. Looking instead at the SNRs with the largest [S II]:H α ratios, the six with [S II]:H $\alpha>1.65$, three are also among the six with the strongest [N II] lines: W21-051, W21-088, and W21-074. The others, W21-025, W21-068, and W21-034, also have strong [N II] lines, [N II]:H $\alpha>2.8$. The ones with the strongest [S II] lines have a wider range of sizes than the [N II]-strongest ones, $10 \, \mathrm{pc} < d < 37 \, \mathrm{pc}$, and they are somewhat less concentrated near the center of M51: only three are at R<2 kpc, though all are at R<4 kpc.

In stark contrast to the SNRs, in the right panels of Figures 6 and 7 we see that the H II regions do *not* show a similar line gradient or scatter with GCD. Indeed, in analyzing the actual abundances of H II regions in M51, Bresolin et al. (2004) find quite modest overall abundance levels near or below solar and almost no abundance gradient in M51, although they did find that nitrogen was somewhat enhanced relative to O: N/O \simeq +0.3 dex, relative to the solar value. So what is the cause of such elevated and variable forbidden-line strengths in the SNR population?

The uncertainties for most of the line fluxes were limited by the background sky subtractions. While it is difficult to quantify these, we investigated qualitatively our background subtractions for the most extreme cases. If $H\alpha$ was being over

or undersubtracted significantly on an object-by-object basis, this could impact the ratios to ${\rm H}\alpha.$ Our inspection of the 2D spectra, however, provides confidence that this is not the case to any significant extent. Even for the object with the single most extreme [N II]:H α ratio (W21-088), we find the background subtraction to have been nominal. The vast majority of the spectra are well detected in the red, and low signal-to-noise ratio or poor sky subtraction cannot explain the observed line ratios. We also note that the H II region sample, processed in the same manner as the SNR sample, shows no such effect.

Could variations in abundances be responsible for the unusually strong lines? The smaller SNRs are almost certainly younger than the larger ones and have consequently swept up less interstellar material. If many of these smaller/younger remnants encounter circumstellar shells, enriched in N as a result of He-burning and shed during the red giant and/or asymptotic giant branch phases of their progenitors' evolution, this would naturally lead to the strong [N II] lines we observe. However, any impact from this effect would be expected only for the very smallest/youngest SNRs. As the left panel of Figure 6 shows, the effect is present for objects as large as 40-50 pc—surely not very young objects. Furthermore, the H II region sample is well behaved and shows no hint of any large N abundance variations from object to object. While this might have been masked in previous studies that have observed giant H II region complexes, our H II region sample includes many smaller, compact HII regions and ones directly adjacent to many of the SNR candidates themselves. If large local variations in abundances were present, our H II sample might be expected to show it, yet it does not.

Less extreme versions of this effect for SNR samples in other galaxies have been attributed to variations in the shock conditions from object to object. There are many parameters that can be varied in shock models (e.g., magnetic field, preshock density, precursor emission, shock completeness, in addition to abundances), and perhaps some combination of parameter variations could be responsible for the observed effect. The more extreme variations seen in M51 SNRs have caused us to revisit this idea in more detail and to conclude that within the context of currently published models it appears difficult to account for the observations.

We have used the extensive grid of shock models from Allen et al. (2008) to investigate the variations in [N II]: $H\alpha$ and [S II]: $H\alpha$ for the broad range of the parameter space covered by the grid, as shown in Figure 8. This grid includes both models with and without self-consistent pre-ionization, over a velocity range from 100 to 1000 km s⁻¹, and over a broad range of assumed preshock densities and magnetic field strengths. Additionally, the grid covers three separate abundance sets, characteristic of the LMC, solar, and 2× solar abundances. Our inspections of these models find no cases where the expected [N II]: $H\alpha$ ratio exceeds a value of 2, let alone our observed values for many objects up to 4 and above. Indeed, the $2 \times$ solar-abundance models actually have somewhat lower ratios than the solar models; apparently, raising the overall abundances affects the cooling carried in various lines, with an overall effect of lowering the [N II]: $H\alpha$ ratio. Figure 9 shows a plot of [N II]: $H\alpha$ versus/[S II]:H α for several other galaxies in addition to M51, emphasizing M51's extreme nature.

The model grids tend to hold one parameter constant while varying other parameters. While it could be true that varying multiple parameters all in the direction that seems to increase

¹⁵ Abundance analyses in M51 using strong-line diagnostics have shown a range of results. However, Bresolin et al. (2004) obtained electron temperatures directly and thus improved (over previous work) abundance determinations; their work is what we reference here. Croxall et al. (2015) carried out an analysis similar to that of Bresolin et al. (2004) for more H II regions in M51 and reached similar conclusions, though they did measure a modest N/O abundance gradient.

Table 5Spectra of SNR Candidates

Name	Hα Flux ^a	$_{\mathrm{H}\beta}$	[O III] $\lambda 5007$	$H\alpha$	[N II] λ6584	[O I] λ6300	[S II] λ6716	[S II] λ6731	[S II]: $\mathrm{H}\alpha$
W21-006	13	71	•••	300	107		47	34	0.27
W21-010	41	96		300	131		59	43	0.34
W21-011 W21-012	60 26	84 74	102 83	300 300	261 261	51 40	62 113	75 80	0.45 0.64
W21-012 W21-013	58	70	100	300	310	~61	145	114	0.86
W21-013 W21-017	123	70	79	300	203	30	95	70	0.55
W21-020	35	32		300	155	~60	83	61	0.48
W21-021	127	31		300	147		62	48	0.37
W21-025	9	143	275	300	635	124	382	271	2.18
W21-027	32	61	207	300	298	32	114	78	0.64
W21-029	6	20	135	300	512	152	222	181	1.34
W21-032	5	•••	196	300	648	~75	103	141	0.81
W21-033	88	42	16	300	171	~22	87	65	0.51
W21-034	9		396	300	752	~110	279	223	1.67
W21-035	126	52	70	300	183	~9	80	62	0.48
W21-037 W21-038	39 6	56 225	20 410	300 300	239 446	45 	127 232	95 174	0.74 1.35
W21-038 W21-040	98	\sim 225 77	132	300	256	24	73	66	0.47
W21-040 W21-042	98 17	70	272	300	505	~54 ~54	176	112	0.47
W21-042 W21-044	20	~35	~61	300	286	120	194	170	1.21
W21-051	24	17	108	300	830	116	310	256	1.89
W21-052	24	46	68	300	505	92	208	173	1.27
W21-058	51	58	123	300	299	26	116	88	0.68
W21-060	14	91	426	300	372		147	133	0.93
W21-062	76	68		300	123		60	38	0.33
W21-064	10		414	300	953	91	188	226	1.38
W21-068	7	69	413	300	767	66	309	220	1.76
W21-069	18	\sim 60	112	300	560	~95	240	177	1.39
W21-070	31	90	271	300	690	79	160	165	1.08
W21-074	42	61	156	300	870	88	268	230	1.66
W21-080	13	45	189	300	771	107	206	164	1.23
W21-084	8	~18	256	300	523	82	177	141	1.06
W21-085 W21-088	103 14	52 ∼43	97 188	300 300	853 1420	84 ∼77	184 293	203 251	1.29 1.81
W21-089	41	~43 51	98	300	411	~// 90	226	187	1.38
W21-009 W21-094	36	104	154	300	317	~27	98	76	0.58
W21-095	58	49	60	300	215		102	76	0.59
W21-098	33		31	300	460	39	126	103	0.76
W21-101	67	26	70	300	438	51	87	99	0.62
W21-103	59	37	157	300	777	45	143	144	0.96
W21-104	56	70	48	300	253	60	150	120	0.90
W21-106	3	\sim 145	315	300	835	436	253	188	1.47
W21-108	38	49	134	300	413	~99	196	182	1.26
W21-118	40	85	20	300	202	41	118	89	0.69
W21-123	38	21	54	300	729	127	226	264	1.63
W21-124	276	56	49	300	163	~7	60	41	0.34
W21-125	15	167	192	300	480	27	195	133	1.09
W21-128 W21-132	14 17	67 42	225	300 300	617 314	211 50	178 128	234 112	1.38 0.80
W21-132 W21-134	134	42 71	173	300	308	35	100	93	0.64
W21-134 W21-135	10	51	156	300	483	101	195	146	1.14
W21-133	19	86	57	300	228		144	101	0.82
W21-133	20	78	286	300	643	61	242	190	1.44
W21-147	37	92	156	300	384	54	174	131	1.02
W21-148	149	73	28	300	139	~16	76	59	0.45
W21-152	14	70	180	300	514	~109	172	148	1.07
W21-155	14	~60	263	300	647	~118	137	146	0.94
W21-161	71	97	133	300	211	38	130	115	0.82
W21-162	28	91	469	300	371	~21	168	120	0.96
W21-164	124	64	101	300	294	46	136	103	0.80
W21-167	26	101	128	300	295	70	89	113	0.67
W21-169	19	77	383	300	311	27	111	105	0.72
W21-172	24	68	176	300	403	87	95	92	0.62

Table 5 (Continued)

Name	$H\alpha \ Flux^a$	$H\beta$	[O III] λ5007	$H\alpha$	[N II] λ6584	[O I] λ6300	[S II] λ6716	[S II] λ6731	[S II]: $H\alpha$
W21-173	109	95	53	300	195	24	92	72	0.55
W21-177	31	58	114	300	254	\sim 45	158	120	0.93
W21-179	185	33	14	300	109	•••	52	38	0.30

Note.

Table 6
Spectra of H II Regions

Name	$H\alpha$ Flux ^a	$H\beta$	[O III] $\lambda 5007$	$H\alpha$	[N II] $\lambda 6584$	[O I] $\lambda 6300$	[S II] $\lambda 6716$	[S II] $\lambda 6731$	[S II]: $H\alpha$
HII-01	1709	49	39	300	107		29	21	0.17
HII-02	598	46	45	300	108		28	20	0.16
HII-03	68	79		300	147		41	25	0.22
HII-04	2014	70	14	300	119	•••	27	19	0.15
HII-05	145	63	~6	300	107		36	26	0.21
HII-06	44	36		300	98		20	21	0.14
HII-07	299	60	55	300	142		18	15	0.11
HII-08	57	34		300	134		19	13	0.10
HII-09	4945	68	5	300	98	2	30	22	0.18
HII-10	80	64		300	79		24	19	0.14
HII-11	11	55		300	91		28	35	0.21
HII-12	125	34		300	89		36	24	0.20
HII-13	179	71		300	70		16	12	0.09
HII-14	209	69	33	300	135		56	38	0.31
HII-15	223	53	42	300	110		27	19	0.16
HII-16	20	45	~16	300	109		21	16	0.12
HII-17	61	49		300	82		26	18	0.15
HII-18	67	40		300	132	~6	24	18	0.14
HII-19	90	39	~9	300	129	~15	58	41	0.33
HII-20	143	77	25	300	119		28	19	0.16
HII-21	27	59		300	107		24	18	0.14
HII-22	32	60		300	98		27	17	0.15
HII-23	1065	41	6	300	87	5	27	21	0.16
HII-24	327	75	~10	300	58		19	14	0.11
HII-25	130	65	24	300	52		20	18	0.13
HII-26	2152	65	4	300	78	3	24	18	0.14
HII-27	188	49		300	65		19	13	0.11
HII-28	277	76	22	300	123		26	18	0.15
HII-29	157	68		300	102		32	23	0.18
HII-30	151	52	~9	300	135		38	25	0.21
HII-31	24	56		300	106		54	38	0.31
HII-32	347	69	~3	300	87		37	28	0.22
HII-33	57	63		300	126		33	25	0.19
HII-34	182	56		300	116		35	25	0.20
HII-35	1522	104	21	300	189	8	34	24	0.19
HII-36	1759	74	14	300	124	1	21	15	0.12
HII-37	190	73		300	113		34	22	0.12
HII-38	6424	57	8	300	114		30	22	0.19
HII-39	283	76	17	300	127	8	29	22	0.13
HII-40	871	66	28	300	130	3	51	27	0.17
HII-40	194	64	10	300	129	~4	22	16	0.20
HII-42	724	26	16	300	145		37	27	0.13
HII-42	117	46	41	300	127		37	25	0.21
HII-43	1157	60	38	300	133	2	27	22	0.20
HII-44	899	34	29	300	124		51	36	0.10
1111-43	899	34	29	300	124	•••	31	30	0.29

Note.

the [N II]:H α and [S II]:H α somewhat might produce higher values of the ratios than seen in the grid, this remains conjecture until such models are actually calculated. One could

also selectively increase the N abundance in the models, but as mentioned above, there is no indication of such an abundance anomaly in the H II sample.

^a Flux in units of 10^{-17} erg cm⁻² s⁻¹.

 $^{^{\}rm a}$ Flux in units of $10^{-17}\,\rm ergs\,cm^{-2}\,s^{-1}.$

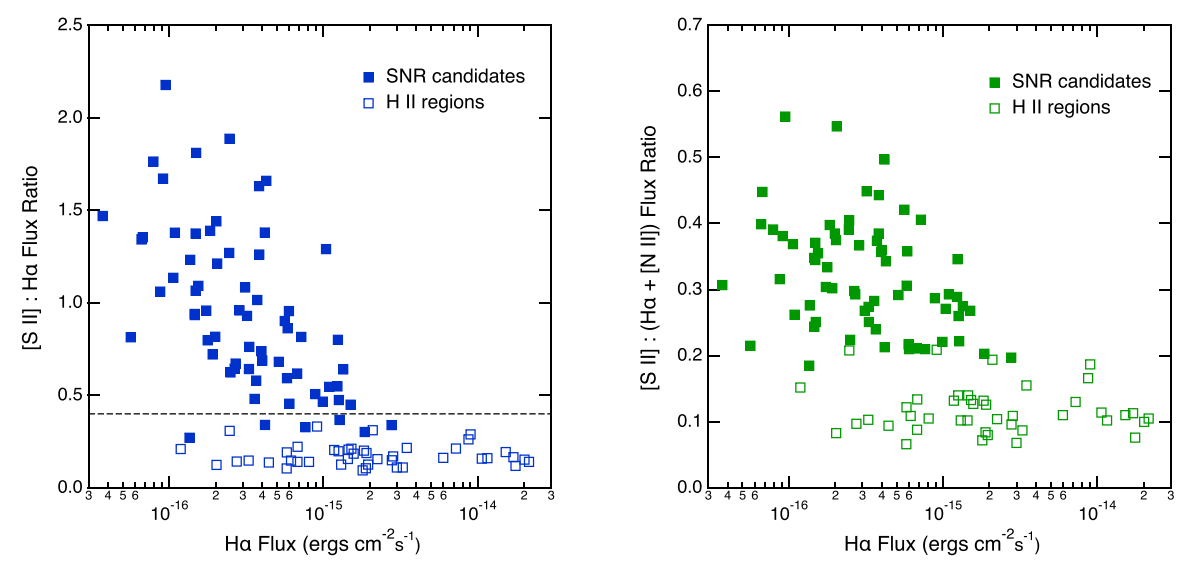


Figure 5. Left: [S II]:H α ratio for the 66 SNR candidates and 44 H II regions for which we obtained GMOS spectra. For 60 of the SNR candidates, the [S II]:H α ratio measured spectroscopically is \geqslant 0.4 (dashed line), so these are almost certainly bona fide SNRs. Meanwhile, the [S II]:H α ratios for all the H II regions are well below 0.4. Right: spectroscopic measurements of the [S II]:(H α + [N II]) ratios for the same objects. This demonstrates the efficacy of selecting candidates using an "H α " filter that also passes the [N II] $\lambda\lambda$ 6548, 6583 lines, as do both the ACS F658N and the GMOS H α one that we used for candidate selection. Both sets of ratios are plotted as a function of H α flux.

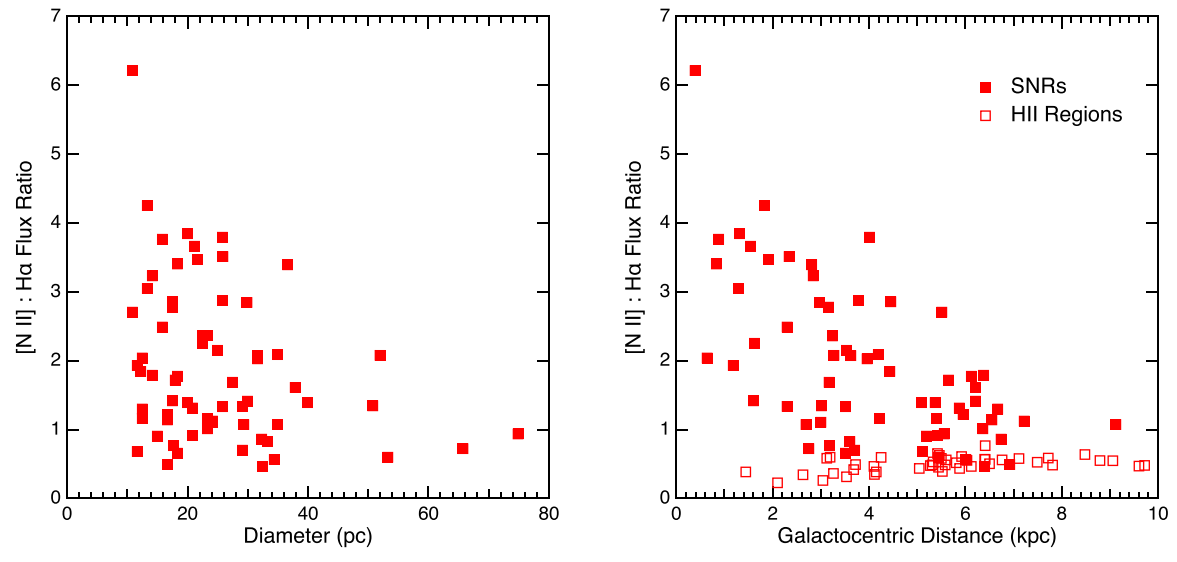


Figure 6. Left: ratio of the nitrogen doublet [N II] $\lambda\lambda$ 6548, 6583 to H α plotted as a function of SNR diameter. Right: same [N II]:H α ratio as a function of GCD. The [N II] lines are extremely strong in the smallest remnants, and they also show a strong gradient with GCD, albeit with large observed dispersion. H II regions do not show a similar gradient, and the ratios are well behaved.

The main difficulty with such elevated ratios is that these singly ionized species are normally formed in about the same temperature zone behind the shock; hence, driving the ratios to widely variable values is difficult. It could be that thermal instabilities in combination with magnetic field or other shock parameters are at play, favoring regions where hydrogen is ionized even as N and S are able to recombine, and thus driving up the observed ratios. However, for these distant SNRs, we are obtaining what are effectively global spectra of their radiative filaments, not localized filaments that might be expected to show such effects more clearly if they were present. It also would not explain why there is such dramatic variation between different objects. Hence, at present we are left with a conundrum.

4.2. Other Emission-line Ratios

The [S II] λ 6717: λ 6731 line ratio is a well-known density diagnostic (e.g., Osterbrock & Ferland 2006). In SNR spectra, this density refers to the density in the postshock recombination zone, but it is related to preshock density (depending on the details of the model assumptions one uses), which in turn is an indication of the interstellar medium (ISM) conditions surrounding each SNR. In the left panel of Figure 10, we show this ratio, and there is a trend toward lower values of the ratio (higher densities) for smaller-diameter (generally younger) objects, but there is significant variation from object to object. This is a pattern we have seen in other galaxies as well, and it is consistent with an interpretation that varying

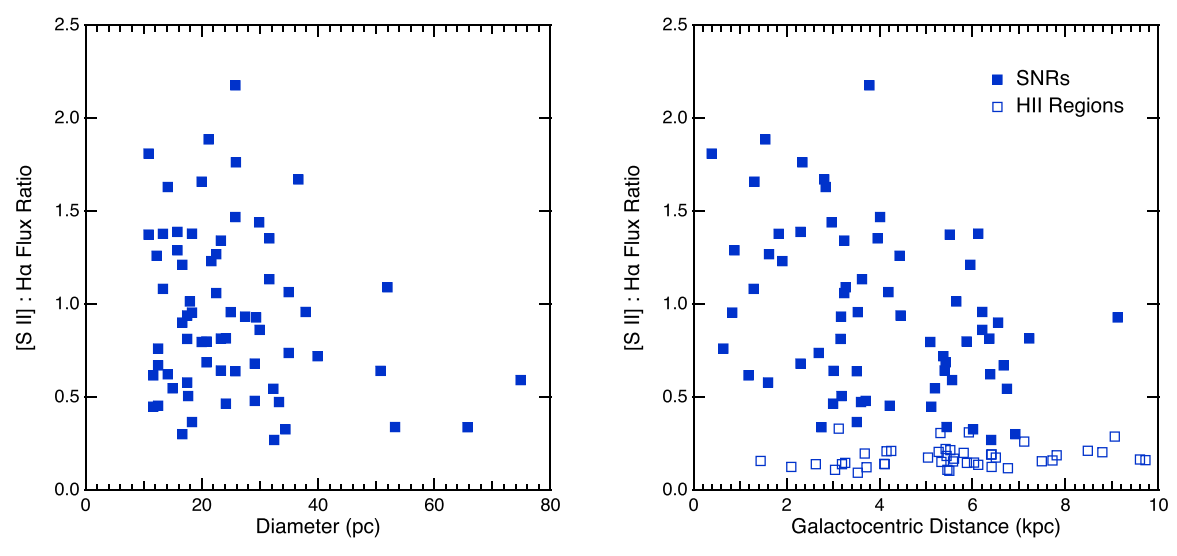


Figure 7. Same as Figure 6, but for the [S II] $\lambda\lambda6716$, 6731:H α ratio. There is a clear gradient with both diameter and GCD (again with large dispersion), but the gradient is not as strong as for the [N II] lines.

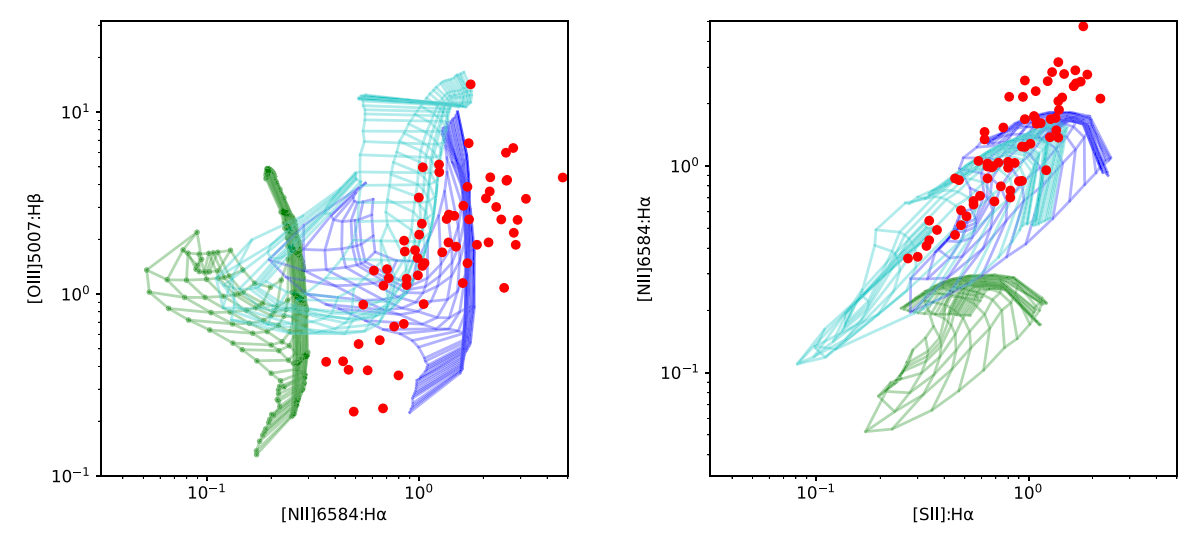


Figure 8. Line ratios we have measured in M51, compared to shock models from Allen et al. (2008) with a range of shock velocities and preshock magnetic fields, and with metallicities corresponding to the LMC (green), solar (blue), and twice solar (cyan). Both plots suggest a range of metallicities for SNRs in M51, from somewhat below to somewhat above Galactic values. However, the objects with the most extreme [N II]: $H\alpha$ ratios are not matched.

conditions in the ISM is a significant driver of the evolution of the SNR sample as a whole.

In the right panel of Figure 10, we show the H β :H α Balmer line ratio, which is nominally an indicator of extinction. Assuming case B, the unreddened ratio would be 0.35, as shown in the figure, with lower values indicating increased extinction. One caveat is that there is a complication with fainter objects and higher extinctions, both of which can make the H β line weaker and more uncertain, thus affecting the measured ratio. The few values above 0.35 are unphysical and are likely afflicted by this effect. Objects with lower ratios may have weak, poorly determined H β values, and hence uncertain (but high) extinction. However, for well-measured objects, the figure shows significant variation, with the lowest ratios indicating E(B-V) values of ~ 1.5 . Similarly, Calzetti et al. (2005) found a high dispersion for H II-emitting knots in M51, especially near the center of the galaxy. Since most of the SNRs are found within the spiral arms and dust lanes, this variation is not surprising, and it is similar to what is observed in other spiral galaxies.

4.3. Sources Identified at X-Ray and Radio Wavelengths

SNRs emit radiation over a wide wavelength range. In M33, for example, where 217 SNRs have been identified, 155 were detected at radio wavelengths by White et al. (2019) in a deep survey carried out with the Jansky Very Large Array. Additionally, 112 were detected (with $>3\sigma$) at X-ray wavelengths, with either XMM-Newton (Garofali et al. 2017) or Chandra (Long et al. 2010), and 98 SNRs were detected in all three bands. Similarly, in M83, where 304 SNRs and SNR candidates have been compiled (Dopita et al. 2010; Blair et al. 2012, 2014), 64 were detected by Russell et al. (2020) in unconfused regions of a radio image created from data obtained with the Australia Telescope Compact Array. A total of 87 of the SNRs in M83 have been detected using Chandra (Long et al. 2014).

M51 has, of course, also been studied at radio and X-ray wavelengths. Maddox et al. (2007) compiled a catalog of 107 compact radio sources using the Very Large Array (VLA), identifying five as likely SNRs, based on their nonthermal

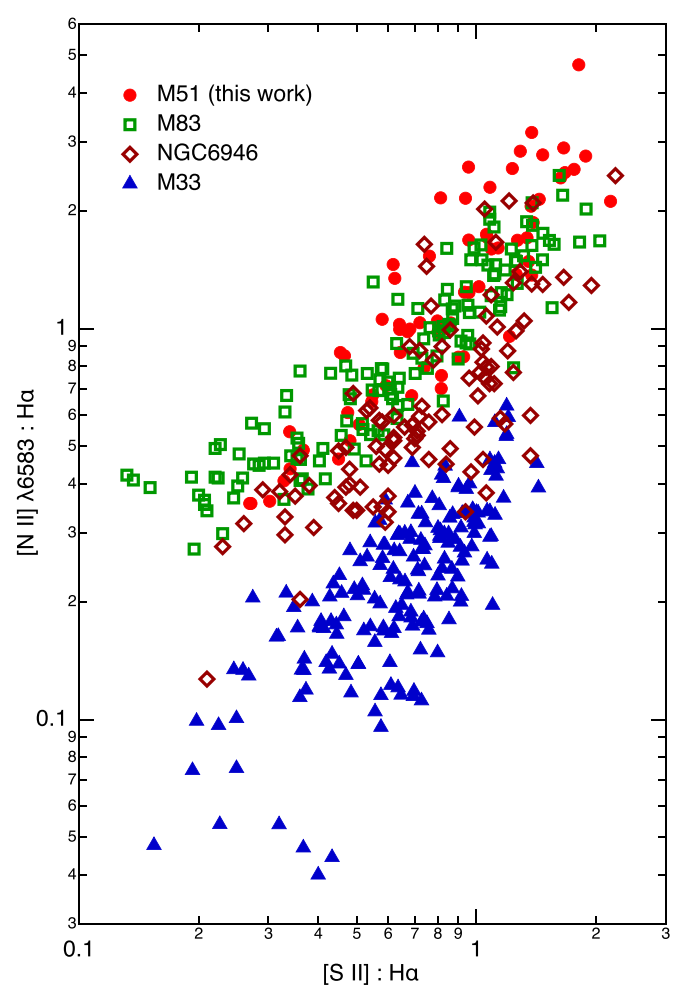


Figure 9. [N II] $\lambda 6583:$ H α flux ratio plotted against the [S II] $\lambda \lambda 6716$, 6731: H α ratio for SNRs in several spiral galaxies. References: M33—Long et al. (2018); M83—Winkler et al. (2017); NGC 6946—Long et al. (2019). The same plot for M51, with models overlaid, is shown in the right panel of Figure 8.

spectral indices and association with resolved shells in ${\rm H}\alpha$ images obtained with HST. Kilgard et al. (2005) gave a catalog of 116 X-ray sources from Chandra observations of M51, and Kuntz et al. (2016) reported a catalog of 297 X-ray sources within the D25 contour for M51 in a much deeper Chandra image of the galaxy. Both these papers suggested that a substantial number of the sources with soft X-ray hardness ratios were likely SNRs. With our data, we can shed additional light on these.

We have investigated positional coincidences of sources from both the Maddox radio and Kuntz X-ray catalogs with the 179 objects we have identified as SNRs or SNR candidates (Table 3). There are 16 radio sources that lie within 1" of one of our SNR candidates, compared with three expected by chance. 16 These include four of the five radio sources identified by Maddox et al. (2007) as probable SNRs. There are 55 X-ray sources that lie within 1" of an SNR candidate, compared with four expected by chance. Of the 16 optical—radio coincidences, 15 are triple coincidences with an X-ray source as well. The

identification of an X-ray and/or radio source at the position of one of the optical SNR candidates clearly increases the likelihood that the object is a bona fide SNR.

Most X-ray sources in deep X-ray studies of nearby galaxies are black-hole or neutron-star binaries, or background AGNs—all sources with hard X-ray spectra. In contrast, SNRs emit X-rays from shock-heated gas and typically have soft X-ray spectra. The two types of objects can be isolated in X-ray hardness-ratio diagrams. As shown in Figure 11, most of the X-ray sources that are spatially coincident with nebulae in our SNR candidate catalog lie in the region where soft X-ray photons dominate, as expected.

We have also turned this technique around and asked what are the other soft X-ray sources in Figure 11. Is there optical evidence of possible SNR emission at those locations? We projected the previously unidentified soft-source positions (those with (M-S)/Total values <-0.5) from Kuntz et al. (2016) onto our HST and GMOS images and performed a visual search for objects of interest. The majority of these positions were empty or were projected onto general star fields in M51. If these are SNRs, then the SN must have occurred in a sparse region of the ISM with few dense cloudlets, thus producing no bright optical remnant. This may favor an SN Ia origin, since the time delay between star formation and SN explosion is generally longer for SNe Ia than for core-collapse SNe (e.g., Totani et al. 2008). Nine additional X-ray sources do have coincident emission nebulae and are thus of possible interest; these are listed in Table 7.

A selection of these objects is shown in Figure 12. Three of the objects could be bona fide SNRs with elevated [S II]: $H\alpha$ ratios, such as X-336, shown in the top panels. Several of the objects found are very small-diameter emission nebulae with relatively low [S II]: $H\alpha$ ratios, as in X-269 (middle panels), but the presence of the soft X-ray counterpart certainly makes them intriguing. Two objects are fainter, more extended nebulae that show some clumpiness or other structure, such as X-317 (bottom panels), but it is difficult to measure accurate ratios from the imagery. Finally, one object is just south of the active nuclear region and aligned with a complex and very extended region of emission; while shocks may be involved in this region, it is unlikely to be an SNR in the sense of the other objects we have found.

We have also checked other sources identified by Maddox et al. (2007) as possible radio SNRs but that are not included in Table 3. There are only two of these: M07-073 and M07-076. As shown in Figure 13, both of these objects have coincident nebulosity, not only in H α but in [S II] as well, though both have nominal [S II]:H α (really [S II]:(H α + [N II]) ratios of \sim 0.15–0.17, somewhat lower than for most of the SNRs in our sample (Figure 5, right). The source M07-073 is also coincident with the soft X-ray source X271, enhancing the likelihood that it is, indeed, an SNR. Information about these two sources is also given in Table 7.

At the very least, these comparisons hint at the incompleteness of our current catalog, which is not surprising in the case of M51, since it is the most distant galaxy for which an extensive search for SNRs has so far been carried out.

 $[\]overline{\ }^{16}$ We estimate chance coincidences by shifting the source positions of one of the catalogs by several arcseconds in various directions and recalculating the number of coincidences. We also allow for a small systematic offset (<0.%3) in position between any two catalogs when carrying out the matching.

 $[\]overline{^{17}}$ Maddox et al. (2007) identified M07-076 as a probable SNR based on its radio spectral index and association with an Hlpha nebula. M07-073 also has a slightly nonthermal spectral index (-0.19 ± 0.30), but it had been identified as a likely SNR in the Chandra survey of M51 by Kilgard et al. (2005).

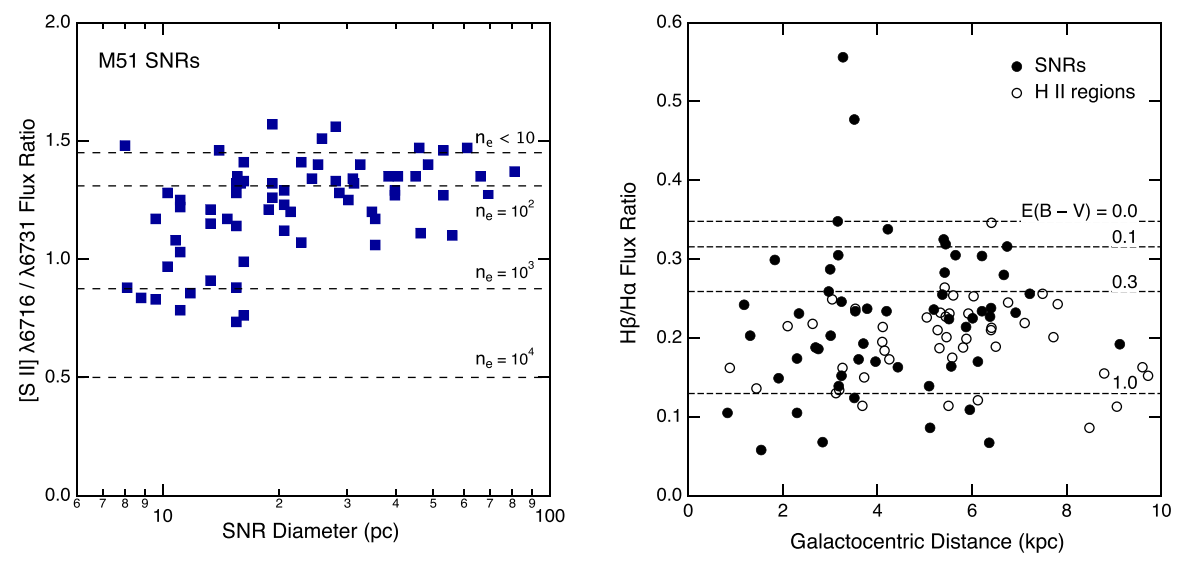


Figure 10. Left: density-sensitive [S II] λ 6717: λ 6731 flux ratio (Osterbrock & Ferland 2006), as a function of the SNR diameter. Not surprisingly, the smaller (and hence probably younger) objects generally have higher densities. Right: H β :H α flux ratio as a function of GCD, for both SNRs and H II regions in M51. The dashed lines indicate various color excess values. The relatively high absorption is not surprising, since both SNRs and H II regions are predominantly located in M51's dusty spiral arms.

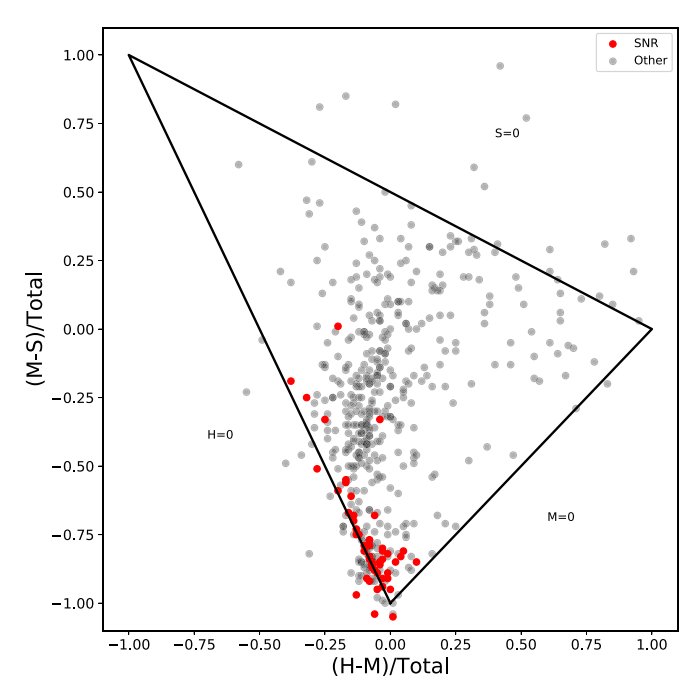


Figure 11. X-ray color–color diagram of X-ray sources in M51, where the soft (S), medium (M), and hard (H) bands correspond to energies of 0.35–1.1 keV, 1.1–2.6 keV, and 2.6–8 keV, respectively, and "Total" is the sum of all three bands. X-ray sources lying within 1" of SNRs or SNR candidates from Table 3 are shown in red, while others are in gray. Not surprisingly, those associated with SNRs are concentrated in the "soft" region of the diagram (lower vertex of the triangle).

Finally, we mention that M51 is host to a number of ultraluminous X-ray sources (ULXs), some of which show eclipses, and others show variability (Terashima & Wilson 2004; Urquhart et al. 2018; Brightman et al. 2020). The numbering of these sources among various authors and the accuracy of the coordinates given are not always clear. However, projecting those nominal sources onto our data (including the Chandra data), we find two objects of likely interest. Urquhart et al. (2018) source ULX-1 corresponds to

our source W21-004, a very elongated optical nebula with elevated [S II]:H α . Urquhart et al. (2018) show a spectrum and conclude that this is a shock-heated jet from the ULX, with some weaker lines possibly indicating some X-ray photoionization as well. By way of comparison, their ULX-2 is also surrounded by a faint semicircular nebula, but their spectrum in this case indicates a much lower [S II]:H α ratio and normal stellar photoionization.

From Brightman et al. (2020), the source they list as ULX-2 is near our source W21-011, but the coordinate given is significantly off. However, projecting onto the Chandra images shows the very bright X-ray source (also Terashima & Wilson 2004 source 5) to be aligned with W21-011, so the coordinate accuracy in Brightman et al. (2020) may be suspect. The optical source in this case is compact and circular, not jet-like. Our spectrum of this source shows [S II]:H α = 0.45 and a fairly high density from the λ 6717: λ 6731 ratio of 0.85 (\sim 1000 cm⁻³). It is not clear whether this source is an SNR with very bright soft X-ray emission or whether the source is more similar to Urquhart et al. (2018) ULX-1 mentioned above but with a different geometry.

Of the remaining ULXs listed by Brightman et al. (2020), ULX-9 is not within our field of view, but none of the others align even approximately with any of our sources. Although we retain W21-004 and W21-011 in our catalog, the exceedingly strong X-ray emission from these two sources makes it clear that they are not normal SNRs per se, but the [S II]:H α ratio criterion found them anyway. This is directly analogous to the situation in M83, where the jet-like microquasar MQ1 was initially associated with an SNR candidate (Soria et al. 2014), and where a second nebula with elevated [S II]:H α may align with another microquasar (Soria et al. 2020).

4.4. Historical Supernovae

While M51's four historical SNe within the past 75 yr (SN 1945A, SN 1994I, SN 2005cs, and SN 2011dh) may not be remarkable in an absolute sense, it does place M51 among the top five galaxies within 10 Mpc in SN productivity. The only

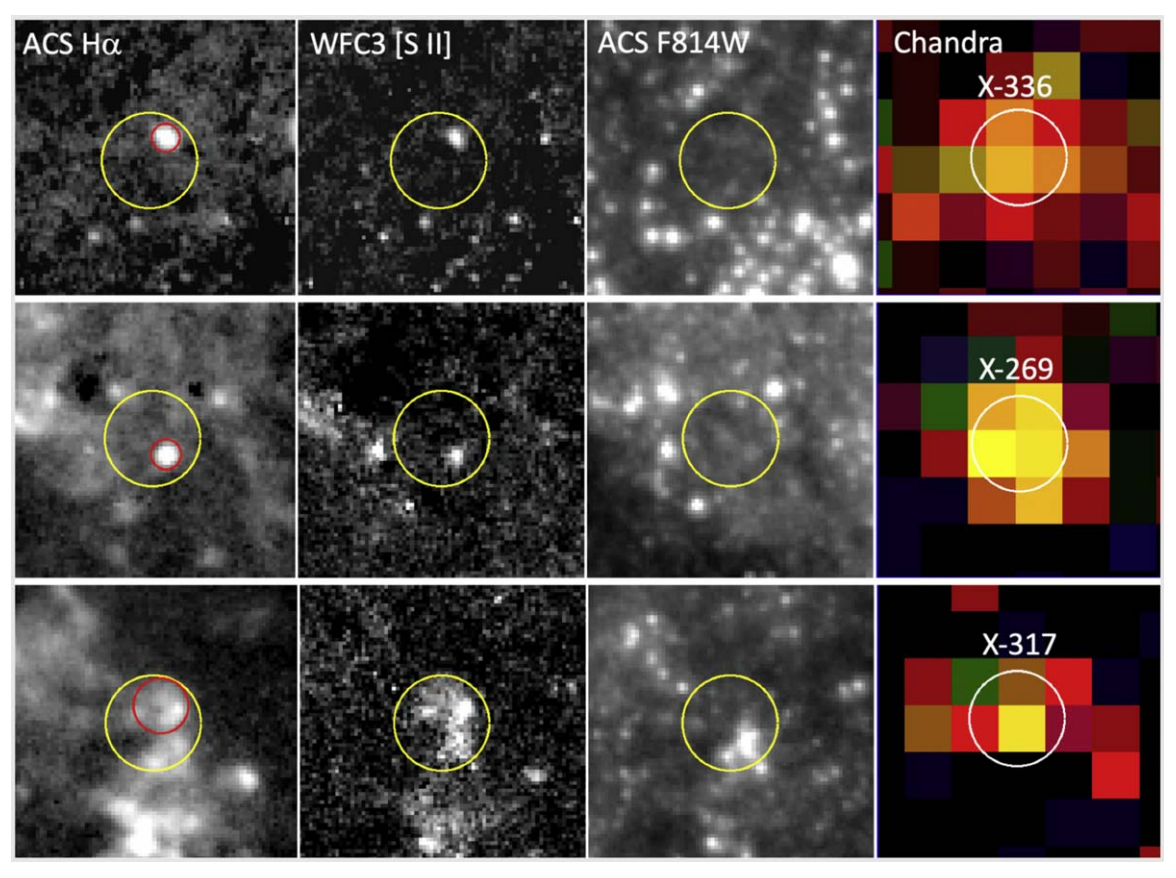


Figure 12. HST and Chandra images of several of the optical objects found to align with soft X-ray sources: X-336, X-269, and X-317. From left to right are the HST H α , [S II], and F814W (*I*-band) continuum; the right panels show Chandra soft (0.35–1.1 keV) in red and medium (1.1–2.6 keV) in green. The yellow circles are 1" in diameter, and the images are oriented north up, east to the left; the smaller red circles in the left panels mark the optical counterparts, all of which are relatively free of continuum contamination.

Table 7Additional M51 Soft X-Ray or Radio Source Matches^a

X-Ray/Radio ID ^b	R.A. (J2000)	Decl. (J2000)	Diam. (pc)	R (kpc)	Comments
		Soft X-ray Sources			
X-145	13:29:46.34	+47:11:15.1	19	3.1	Likely SNR
X-164	13:29:50.08	+47:11:39.5	6	1.2	Modest [S II]: $H\alpha$, possible SNR
X-211	13:29:52.76	+47:11:40.0	49	0.1	Blowout, S of nucleus
X-224	13:29:53.54	+47:11:26.5	5	0.8	Modest [S II]: $H\alpha$, possible SNR
X-269	13:29:55.44	+47:11:43.5	6	1.2	Modest [S II]: $H\alpha$, possible SNR
X-317	13:29:59.57	+47:11:11.6	24	3.4	Ill-defined; possible SNR
X-336	13:30:01.10	+47:13:32.9	7	5.9	Likely SNR
X-359	13:30:04.32	+47:08:41.3	65	9.3	Large shell, GMOS, likely SNR
X-368	13:30:05.06	+47:10:35.9	24	6.3	Likely SNR
		Radio Sources			
M07-073	13:29:55.41	+47:14:01.9	17.5	5.9	X271; modest [S II]: $H\alpha$, likely SNI
M07-076	13:29:55.60	+47:12:02.9	18.7	1.5	Modest [S II]: $H\alpha$, possible SNR

Notes

one of M51's historical SNe detected in the images discussed here is the Type IIb SN 2011dh, located in the galaxy's outer spiral arm, \sim 2.6 SE of the nucleus. The declining SN is shown in the [S II] and F689M images from 2012, over 10 months

after the explosion (Figure 14, panels (b) and (c)). The progenitor candidate was first identified by Li et al. (2011b) and is discussed by Van Dyk et al. (2011). Figure 14(a) shows the progenitor (or more likely its brighter companion; see Van Dyk

^a Positions and sizes are for the associated optical counterpart to the X-ray or radio source.

 $^{^{\}rm b}$ X-ray IDs from Kuntz et al. (2016); radio IDs from Maddox et al. (2007).

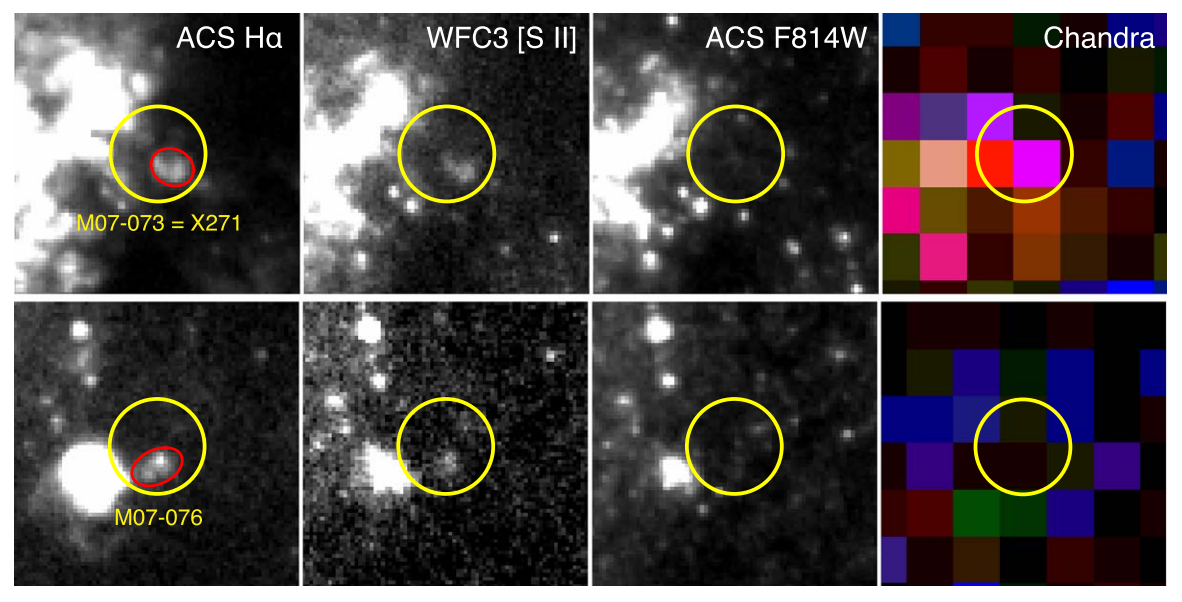


Figure 13. HST and Chandra images of the optical objects found to align with radio sources 73 and 76 from the catalog of M51 sources by Maddox et al. (2007). Panels are similar to those in Figure 12: left to right are the HST H α , [S II], and F814W (*I*-band) continuum; the right panels show Chandra 0.35–1.1 keV in red, 1.1–2.6 keV in green, and 2.6–8.0 keV in blue. The yellow circles are 1" in diameter, and the images are oriented north up, east to the left; the smaller red ellipses in the left panels mark the optical counterparts, both of which are relatively free of continuum contamination.

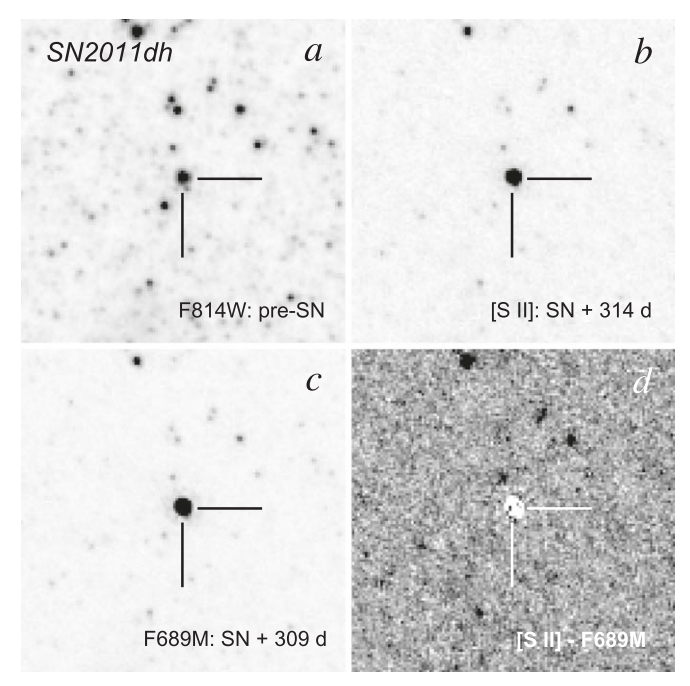


Figure 14. HST images showing the position of SN 2011dh: (a) red continuum (F814W) about 6 yr prior to the SN explosion (this is the same data shown in Van Dyk et al. 2011, Figure 1); (b) image in [S II] (F673N) about 10 months post-explosion; (c) F689M band about 10 months post-explosion; (d) difference image between [S II] and F689M. The SN is somewhat oversubtracted, yet residuals remain for several stars, indicating the absence of [S II] nebular emission from SN 2011dh. The field size is 5", oriented north up, east to the left; the tick marks indicate the SN position and are 1" in length.

et al. 2011) in the 2005 data. By taking a difference image between the [S II] image and the F689M image from our 2012 data (Figure 14(d)), we see that the SN itself appears somewhat oversubtracted, while residuals from several stars remain visible. This indicates that no nebular emission (at least in the [S II] lines) had developed at the time these images were

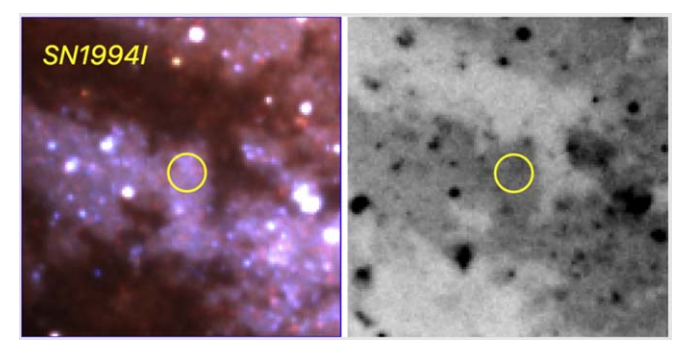
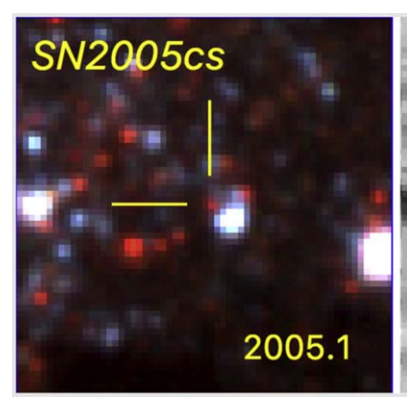


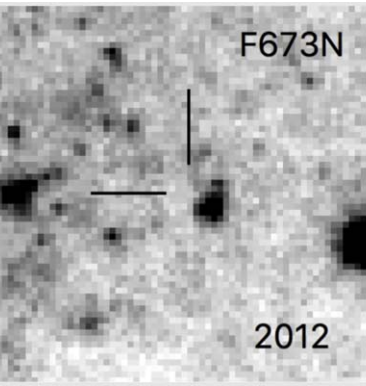
Figure 15. HST ACS images from 2005 showing the position of SN 1994i: color image where R = F814W, G = F555W, B = F435W (left); F658N (H α + [N II]) (right). The field is 5' square, oriented north up, east to the left. The circle marks the SN location and is 0."6 in diameter, indicating the 3σ uncertainty in the SN position. No nebular remnant is apparent at this position.

taken, 10 months post-explosion. The late-time evolution of SN 2011dh is discussed in detail by Maund (2019).

We have also examined the positions of the other three historical SNe. The Type I SN 1945A took place in M51B = NGC 5195, at a location only about \sim 7" SW of the bright nucleus, with a large uncertainty in its position. Nothing stands out in the HST ACS images (the only ones to cover this crowded field). SN 1994I (Type Ic) was located 18" SE from the nucleus of M51A, also in a crowded field. Figure 15 shows the ACS images of this field; there is no evidence for nebulosity that might indicate a remnant from SN 1994I.

SN 2005cs (Type IIP) exploded on 2005 June 26, about 5 months after the HST ACS images in program 10452 (Table 1) were taken. In Figure 16, the left panel shows a three-color image from 5 months prior to the event in which the red supergiant progenitor identified by Li et al. (2006) is marked. This star is apparently missing in the middle panel, showing the [S II] (F673N) image from 2012. The right panel shows a continuum-subtracted $H\alpha$ image (ACS F658N–WFC3 F689M), which shows two small nebulae just NE and SE of





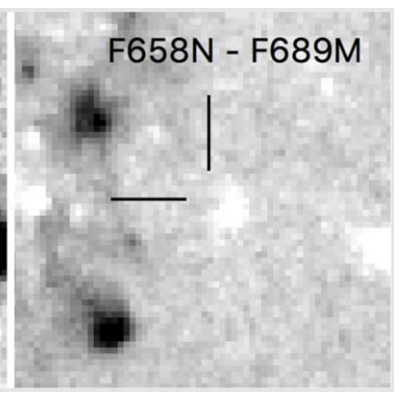


Figure 16. HST images of a 3" square field centered on the location of SN 2005cs. Left: color image where R = F814W, G = F555W, B = F435W, taken 5 months prior to the SN event. The position of the red supergiant identified by Li et al. (2006) as the progenitor star is marked, immediately NE of a bright object that is probably a compact star cluster (the tick marks are 0."5 in length). Li et al. show these same images individually, but with an even smaller field, in their Figure 3. Middle: WFC3 F673N image from 2012, 7 yr after the event. The progenitor star is no longer visible, nor is there any resulting [S II] nebulosity visible. Right: difference image between ACS F658N ($H\alpha + [N II]$) and the WFC3 F689M continuum, clearly showing two small nebulae, unrelated to the SN, about 1" NE and SE from the SN position.

the SN position (also faintly visible in $[S\,II]$ in the middle panel). These are present both before and after the SN event; there is no apparent remnant from the SN itself.

4.5. Comparison with Other Spiral Galaxies

In recent years, large populations of SNRs have been identified in numerous galaxies, including M31 (Lee & Lee 2014a), M33 (Lee & Lee 2014a; Long et al. 2018), M81 (Lee et al. 2015), M83 (Winkler et al. 2017), and NGC 6946 (Long et al. 2019). How does the population of SNRs in M51 compare with ones in many of these other galaxies?

We show a plot of the cumulative size distribution, N(< D) as a function of the diameter, D, for SNRs in M51, and for three other spiral galaxies with extensive SNR samples, in Figure 17. (Data sources are in the figure caption.) For M51, as for M83 and NGC 6946, all the diameters have been measured from HST images. ¹⁸ The number—diameter distributions for SNRs in other galaxies are similar. For example, Long (2017) shows number—diameter plots for several galaxies, including the SMC and LMC (based on data from Badenes et al. 2010) and M31 (based on data from Lee & Lee 2014a), that resemble those for the galaxies shown here.

It is interesting to note that for all four galaxies in Figure 17, those portions of the distributions with a few to a few tens of objects have slopes approximately consistent with Sedov expansion and a uniform average SN rate, $N(< D) \propto D^{5/2}$; in contrast, one expects $N(< D) \propto D$ for free expansion. In actuality, this result is most likely due to a combination of selection effects rather than something physical. The optical emission that we observe from (most) SNRs arises from relatively low velocity $(100-300\,\mathrm{km\,s^{-1}})$ radiative shocks propelled by the primary shock into dense cloudlets in the ISM. Because the surface area of the primary shock increases with time, we generally expect the optical luminosity to increase with time as well, until the primary shock velocity drops to the point where it can no longer drive secondary

shocks into these cloudlets. We then expect the SNR (now in the so-called radiative phase) to fade.

The maximum luminosity an SNR reaches—and importantly the radius at which it reaches maximum—depends on a variety of factors, including the average density of the ISM, the number of cloudlets, and the energy of the SNR explosion. SNRs expanding into dense media brighten, and eventually fade, at smaller radii than those expanding into less dense material. At some level, the samples of SNRs that we have observed in all of these galaxies are luminosity limited at small diameters and surface brightness limited at large diameters. At the small-diameter end of the distribution, we are unable to measure diameters of unresolved objects, which effectively sets a lower limit at the point-spread function (PSF) of the detector used. Furthermore, SNRs with sizes on the order of the PSF are hard to pick out against stars (because it is difficult to remove stars completely from narrowband images). These two effects limit the low end of the distribution and probably explain why the limits for M51 and NGC 6946 are about twice that for the similar galaxy M83—since the former two galaxies are at almost twice M83's distance.

The number of SNRs in a galaxy should be proportional to the star formation rate (SFR), since about 75% of the SNe observed in external galaxies arise from the core-collapse explosion of massive stars whose main-sequence lifetimes are short (Li et al. 2011a), and since the ages of stellar populations that produce SNe I are also typically less than 1 Gyr (Maoz et al. 2010). The SFRs of the galaxies shown in Figure 17 vary. According to Jarrett et al. (2013), the SFRs for M83, NGC 6946, and M51 are all similar: estimates are in the range of 0.9–3.2 M_{\odot} yr⁻¹, 1.4–3.2 M_{\odot} yr⁻¹, and 1.3–3.5 M_{\odot} yr⁻¹, respectively, depending on the wavelength band used to estimate the SFR.

On the other hand, there have been four historical SNe in M51, whereas M83 and NGC 6946 have hosted 6 and 10, respectively, suggesting that the SFRs in the latter two galaxies are somewhat higher than in M51. For M33, ¹⁹ the SFR is between 0.2 and 0.5 M_{\odot} yr⁻¹. No SN has been observed

 $[\]overline{^{18}}$ For NGC 6946, data are from Tables 1 and 2 of Long et al. (2020). Virtually all diameters were measured from HST images—H α where available, but some objects were detected only in the [Fe II] 1.644 μm line and so were measured on those images. A very few objects lay outside the HST footprint, so those diameters were estimated from ground-based images.

¹⁹ For M33, the SFR is variously estimated by Williams et al. (2018) to be from 0.17 ± 0.06 M_{\odot} yr⁻¹ from a multiwavelength analysis to 0.25^{+0.10}_{-0.07} M_{\odot} yr⁻¹ using FUV and 24 μ m imaging to 0.33 ± 0.10 M_{\odot} yr⁻¹ using SED fitting, whereas Verley et al. (2009) suggest 0.45 ± 0.10 M_{\odot} yr⁻¹ from a multiwavelength analysis.

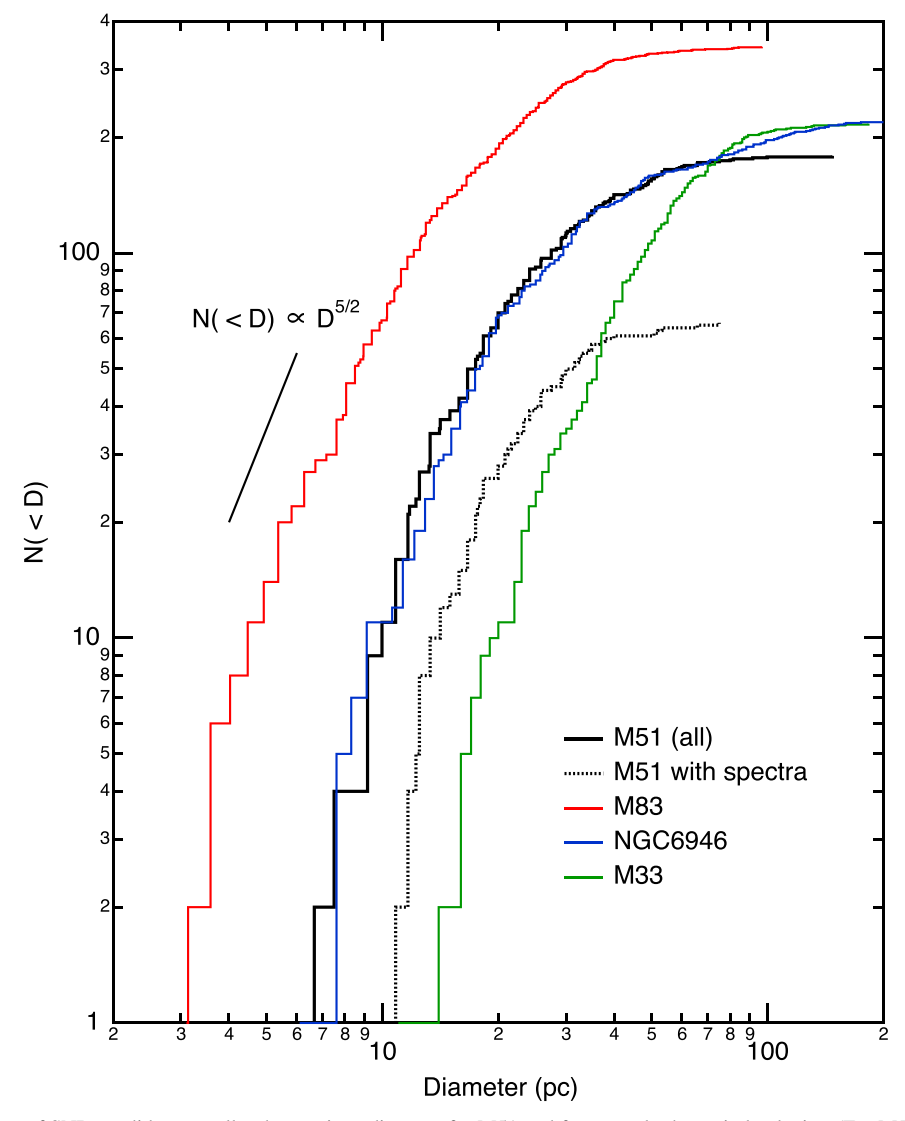


Figure 17. Cumulative number of SNR candidates smaller than a given diameter for M51 and for several other spiral galaxies. (For M51 we show both the complete sample (Table 3) and those for which we have obtained spectra, to demonstrate that those with spectra represent a fair subset of the entire sample.) For each of the galaxies, the heart of the distribution, where there are a few dozen SNRs, has a slope consistent with Sedov expansion $(D(t) \propto t^{2/5})$, so $N(< D) \propto D^{5/2}$ for a uniform SN rate). References: M83—Blair et al. (2012, 2014); NGC 6946—Long et al. (2020); M33—Lee & Lee (2014b); Long et al. (2018).

historically in M33. Therefore, if all the samples had equal luminosity sensitivity, we might expect there to be roughly equal numbers of SNRs in M83, NGC 6946, and M51, and far fewer in M33. In point of fact, however, there are 300 SNRs (and candidates) in M83, 225 in NGC 6946, 179 in M51, and 217 in M33. The relatively large number of SNRs in M33 is clearly due to its proximity. SNRs exhibit a large range of luminosities at any diameter, and the various SNR samples are mainly flux, not luminosity, limited. M51 is the most distant galaxy in the sample (8.58 Mpc), compared to M83 at 4.6 Mpc (Saha et al. 2006) and NGC 6946 at 7.8 Mpc (Anand et al. 2018; Murphy et al. 2018). As a result, one would expect M51 to have somewhat fewer SNRs in a flux-limited sample.

The biggest difference in the samples is in the number of small-diameter SNRs. M51 and NGC 6946 both have about 10 SNRs with diameters of 10 pc or less, whereas M83 has almost 100, and M33 has none. With a couple of exceptions, all of the small-diameter SNRs in these galaxies were identified on the basis of elevated [S II]:H α ratios, not from properties that one would expect from a young, ejecta-dominated SNR like Cas A.

Also, the [S II]: $H\alpha$ technique cannot find young Balmerdominated SNRs that arise from SNe Ia. Therefore, the most likely reason for this difference is that the small-diameter SNRs that we do detect are ones expanding into locally dense regions of the ISM. M83 is known to have very substantial diffuse soft X-ray emission, indicative of a hot, high-pressure ISM throughout its spiral arms, which may account for the larger number of small-diameter SNRs.

5. Summary

We have used a combination of ground-based and space-based imagery to construct the first catalog of SNRs for M51, based on elevated [S II]:H α line ratios compared to H II regions in the same images. Our list of candidates totals 179 objects. We obtained GMOS spectra of 66 of the candidates (along with a number of H II regions); 60 of the SNR candidates have measured [S II]:H α ratios that exceed 0.4, the standard value for declaring an emission nebula to be an SNR. Moreover, 51 of the candidates show intrinsic [O I] λ 6300, another line

associated with radiative shocks, including one object with a [S II]:H α ratio slightly below the 0.4 limit. This suggests not only that a high percentage of our SNR candidates (61 of 66) are actually SNRs but also that the vast majority of other SNR candidates in our catalog are also likely to be bona fide SNRs.

The SNRs/candidates in the sample are mostly distributed along the very prominent spiral arms of M51. Nearly a third (55) of 179) of the SNRs/candidates are coincident with X-ray sources identified with Chandra (Kuntz et al. 2016), and most of these X-ray sources have the soft spectra normally seen in SNRs. A search at the positions of other soft X-ray sources turned up another handful of possibly interesting candidates. Only 16 of the SNRs/candidates are associated with VLA radio sources cataloged by Maddox et al. (2007), and a search at the positions of additional objects they identified as likely SNRs shows interesting optical emission from two of those. The median diameter of the SNRs in the sample is 24 pc; none of the SNRs for which we have spectra show evidence of the type of peculiar abundances or line broadening expected from a young SNR in the free expansion phase such as Cas A in our Galaxy; most are likely in the Sedov (or possibly radiative) phase of their evolution.

We have detected nebular emission from none of the four historical SNe that have occurred in M51, but we do detect fading continuum from SN 2011dh in HST images taken 10 months after that event.

The most surprising feature of the spectra of the SNRs in M51 is the behavior of the [N II] lines relative to $H\alpha$. We see very high [N II]: $H\alpha$ line ratios in many of them, which, from an observational perspective, explains why the imaging [S II]: $H\alpha$ line ratios for the SNR candidates were lower than typically seen in other galaxies. (That is, the $H\alpha$ filters used passed significant [N II] emission as well, lowering the observed ratio.) Additionally, the dispersion in [N II]: $H\alpha$ between objects of similar size or similar GCD is very large. While both of these effects have been seen in other galaxies, they are more extreme (and hence more obvious) in M51 and seem to be pointing toward something more fundamental.

The cause for such high ratios is hard to explain astrophysically. The highest [N II]: $H\alpha$ ratios tend to appear in smaller-diameter SNRs, or alternatively in objects at relatively small galactocentric radius, but the large dispersion in values seems to indicate that neither of these parameters is a dominant effect. As far as the abundance of N is concerned, the [N II]: $H\alpha$ ratios in M51 are higher on average than in galaxies like M83, where the *overall* metallicity is significantly higher. Existing shock models with elevated abundances do not reproduce the observed [N II]:H α ratios we see in M51 SNRs; furthermore, the [N II]:H α ratios in M51 H II regions are not unusual and are nearly constant with galactocentric radius, as expected from the overall metallicity. Hence, abundance variations do not provide an obvious explanation. Further spectroscopic studies and modeling of the SNRs in M51 are clearly warranted to understand this conundrum.

We thank Derek Hammer (previously of STScI), Heather Greenfield (STScI), and Jennifer Mack (STScI) for producing the aligned, mosaicked HST images and properly applying the CTE corrections to the HST data used in this paper. We are also grateful for valuable comments from John Raymond. Partial support for the analysis of the data was provided by NASA through grant Nos. HST-GO-12762 and HST-GO-15216 from

the Space Telescope Science Institute, which is operated by AURA, Inc., under NASA contract NAS 5-26555. P.F.W. acknowledges additional support from the NSF through grant AST-1714281. W.P.B. acknowledges partial support from the JHU Center for Astrophysical Sciences.

Facilities: HST(WFC3), HST(ACS), Gemini:North (GMOS). Software: astropy (Astropy Collaboration et al. 2013), AstroDrizzle (Gonzaga et al. 2012), matplotlib (Hunter 2007), SAOImageDS9 (Joye & Mandel 2003).

ORCID iDs

P. Frank Winkler https://orcid.org/0000-0001-6311-277X Sadie C. Coffin https://orcid.org/0000-0003-3038-8045 William P. Blair https://orcid.org/0000-0003-2379-6518 Knox S. Long https://orcid.org/0000-0002-4134-864X Kip D. Kuntz https://orcid.org/0000-0001-6654-5378

References

```
Allen, M. G., Groves, B. A., Dopita, M. A., Sutherland, R. S., & Kewley, L. J.
   2008, ApJS, 178, 20
Anand, G. S., Rizzi, L., & Tully, R. B. 2018, AJ, 156, 105
Astropy Collaboration, Robitaille, T. P., Tollerud, E. J., et al. 2013, A&A,
   558, A33
Badenes, C., Maoz, D., & Draine, B. T. 2010, MNRAS, 407, 1301
Blair, W. P., Chandar, R., Dopita, M. A., et al. 2014, ApJ, 788, 55
Blair, W. P., Winkler, P. F., & Long, K. S. 2012, ApJS, 203, 8
Bresolin, F., Garnett, D. R., & Kennicutt, R. C. J. 2004, ApJ, 615, 228
Brightman, M., Earnshaw, H., Fürst, F., et al. 2020, ApJ, 895, 127
Calzetti, D., Kennicutt, R. C. J., Bianchi, L., et al. 2005, ApJ, 633, 871
Croxall, K. V., Pogge, R. W., Berg, D. A., Skillman, E. D., & Moustakas, J.
   2015, ApJ, 808, 42
Dopita, M. A., Blair, W. P., Long, K. S., et al. 2010, ApJ, 710, 964
Fruchter, A. S. E., Hack, W., Dencheva, N., et al. 2010, in 2010 Space
   Telescope Science Institute Calibration Workshop, ed. S. Deustua &
   C. Oliveira (Baltimore, MD: STScI), 382
Gaia Collaboration, Brown, A. G. A., Vallenari, A., et al. 2018, A&A, 616, A1
Garofali, K., Williams, B. F., Plucinsky, P. P., et al. 2017, MNRAS, 472, 308
Gonzaga, S., Hack, W., Fruchter, A., & Mack, J. 2012, The DrizzlePac
   Handbook (Baltimore, MD: STScI)
Hunter, J. D. 2007, CSE, 9, 90
Jarrett, T. H., Masci, F., Tsai, C. W., et al. 2013, AJ, 145, 6
Joye, W. A., & Mandel, E. 2003, in ASP Conf. Ser. 295, Astronomical Data
   Analysis Software and Systems XII, ed. H. E. Payne, R. I. Jedrzejewski, &
   R. N. Hook (San Francisco, CA: ASP), 489
Kilgard, R. E., Cowan, J. J., Garcia, M. R., et al. 2005, ApJS, 159, 214
Kuntz, K. D., Long, K. S., & Kilgard, R. E. 2016, ApJ, 827, 46
Lee, J. H., Hwang, N., & Lee, M. G. 2011, ApJ, 735, 75
Lee, J. H., & Lee, M. G. 2014a, ApJ, 786, 130
Lee, J. H., & Lee, M. G. 2014b, ApJ, 793, 134
Lee, M. G., Sohn, J., Lee, J. H., et al. 2015, ApJ, 804, 63
Levenson, N. A., Kirshner, R. P., Blair, W. P., & Winkler, P. F. 1995, AJ,
   110, 739
Li, W., Chornock, R., Leaman, J., et al. 2011a, MNRAS, 412, 1473
Li, W., Filippenko, A. V., & van Dyk, S. D. 2011b, ATel, 3401, 1
Li, W., Van Dyk, S. D., Filippenko, A. V., et al. 2006, ApJ, 641, 1060
Long, K. S. 2017, Galactic and Extragalactic Samples of Supernova Remnants:
   How They Are Identified and What They Tell Us (Berlin: Springer), 2005,
   doi:10.1007/978-3-319-21846-5_90
Long, K. S., Blair, W. P., Milisavljevic, D., Raymond, J. C., & Winkler, P. F.
   2018, ApJ, 855, 140
Long, K. S., Blair, W. P., Winkler, P. F., et al. 2010, ApJS, 187, 495
Long, K. S., Blair, W. P., Winkler, P. F., & Lacey, C. K. 2020, ApJ, 899, 14
Long, K. S., Kuntz, K. D., Blair, W. P., et al. 2014, ApJS, 212, 21 Long, K. S., Winkler, P. F., & Blair, W. P. 2019, ApJ, 875, 85
Maddox, L. A., Cowan, J. J., Kilgard, R. E., Schinnerer, E., & Stockdale, C. J.
   2007, AJ, 133, 2559
Maoz, D., Sharon, K., & Gal-Yam, A. 2010, ApJ, 722, 1879
Massey, P., Strobel, K., Barnes, J. V., & Anderson, E. 1988, ApJ, 328, 315
Mathewson, D. S., & Clarke, J. N. 1973, ApJ, 180, 725
Matonick, D. M., & Fesen, R. A. 1997, ApJS, 112, 49
Maund, J. R. 2019, ApJ, 883, 86
```

```
McQuinn, K. B. W., Skillman, E. D., Dolphin, A. E., Berg, D., & Kennicutt, R.
  2016, ApJ, 826, 21
Murphy, J. W., Khan, R., Williams, B., et al. 2018, ApJ, 860, 117
```

Osterbrock, D. E., & Ferland, G. J. 2006, Astrophysics of Gaseous Nebulae and Active Galactic Nuclei (2nd ed.; Sausalito, CA: Univ. Science

Rosse, T. E. O. 1850, RSPT, 140, 499

Russell, T. D., White, R. L., Long, K. S., et al. 2020, MNRAS, 495, 479 Saha, A., Thim, F., Tammann, G. A., Reindl, B., & Sandage, A. 2006, ApJS,

Soria, R., Blair, W. P., Long, K. S., Russell, T. D., & Winkler, P. F. 2020, ApJ, 888, 103

Soria, R., Long, K. S., Blair, W. P., et al. 2014, Sci, 343, 1330 Terashima, Y., & Wilson, A. S. 2004, ApJ, 601, 735 Totani, T., Morokuma, T., Oda, T., Doi, M., & Yasuda, N. 2008, PASJ, 60, 1327

Urquhart, R., Soria, R., Johnston, H. M., et al. 2018, MNRAS, 475, 3561 Van Dyk, S. D., Li, W., Cenko, S. B., et al. 2011, ApJL, 741, L28 Verley, S., Corbelli, E., Giovanardi, C., & Hunt, L. K. 2009, A&A, 493,

White, R. L., Long, K. S., Becker, R. H., et al. 2019, ApJS, 241, 37 Williams, T. G., Gear, W. K., & Smith, M. W. L. 2018, MNRAS, 479, 297 Winkler, P. F., Blair, W. P., & Long, K. S. 2017, ApJ, 839, 83 Zacharias, N., Finch, C., Girard, T., et al. 2010, AJ, 139, 2184